

# General Relativistic Magnetohydrodynamic Simulations of Binary Neutron Star Mergers with the APR4 Equation of State

**A Endrizzi, R Ciolfi, B Giacomazzo, W Kastaun, and T Kawamura**

Physics Department, University of Trento, via Sommarive 14, I-38123 Trento, Italy  
INFN-TIFPA, Trento Institute for Fundamental Physics and Applications, via Sommarive 14,  
I-38123 Trento, Italy

E-mail: andrea.endrizzi.2@unitn.it, bruno.giacomazzo@unitn.it

**Abstract.** We present new results of fully general relativistic magnetohydrodynamic (GRMHD) simulations of binary neutron star (BNS) mergers performed with the Whisky code. All the models use a piecewise polytropic approximation of the APR4 equation of state (EOS) for cold matter, together with a “hybrid” part to incorporate thermal effects during the evolution. We consider both equal and unequal-mass models, with total masses such that either a supramassive NS or a black hole (BH) is formed after merger. Each model is evolved with and without a magnetic field initially confined to the stellar interior. We present the different gravitational wave (GW) signals as well as a detailed description of the matter dynamics (magnetic field evolution, ejected mass, post-merger remnant/disk properties). Our simulations provide new insights into BNS mergers, the associated GW emission and the possible connection with the engine of short gamma-ray bursts (both in the “standard” and in the “time-reversal” scenarios) and other electromagnetic counterparts.

Online supplementary data available from [stacks.iop.org/cqg/33/164001/mmedia](https://stacks.iop.org/cqg/33/164001/mmedia)

**Keywords:** numerical relativity, binary neutron stars, gravitational waves, magnetohydrodynamics

PACS numbers: 04.25.dk, 04.30.Db, 04.40.Dg, 97.60.Jd, 97.60.Lf

Submitted to: *Class. Quantum Grav.*

## 1. Introduction

After the recent detection [1] of gravitational waves (GW) from the merger of two black holes (BHs) by the ground-based LIGO interferometers, it seems to be only a matter of time until GWs from merging neutron stars (NS) are detected as well (see [2] for estimated event rates). BNS mergers may also power bright electromagnetic (EM) signals, including short gamma-ray bursts (SGRBs, see [3] for a review). The imminent integration of the Virgo detector into the working GW network will improve the sky localization and enlarge the chances of detecting EM counterparts in the follow-up of a GW detection. Furthermore, the matter ejected during BNS mergers is thought to be responsible, at least partially, for the creation of heavy elements in the universe (see e.g., [4, 5]).

BNS systems can be divided into two main categories: “high-mass” BNSs that form a BH or a hypermassive NS (HMNS) after merger, and “low-mass” BNSs that form instead a long-lived supramassive NS (SMNS) or even a stable NS. An HMNS is an NS whose mass is above the maximum mass for a uniformly rotating NS (hypermassive limit) and that will collapse to a BH in less than  $\sim 1$  second after merger. The BH formed by “high-mass” BNS mergers may be surrounded by an accretion disk, which is thought to be a necessary (however not sufficient) condition to power a relativistic jet and produce an SGRB. Preliminary simulations performed with the `Whisky` code showed the possible formation of a strongly collimated magnetic field along the BH spin axis [6], but a different simulation from another group was not able to produce similar results [7]. The only evidence of jet formation, up to now, has been provided very recently for an equal-mass NS-NS merger [8], following a similar result for an NS-BH merger [9].

An SMNS is an NS with mass above the maximum mass for a non-rotating NS, but below the hypermassive limit. In this case, uniform rotation can be sufficient to support the star against the collapse to a BH. However, on a spin-down timescale (minutes to hours) the star will eventually collapse. Therefore, the merger of a “low-mass” system results in a NS that either collapses on a very long time scale, or does not collapse at all. The observations of  $\sim 2 M_{\odot}$  NSs [10, 11] support the idea that at least a significant fraction of BNS mergers will lead to the formation of SMNSs or even stable NSs. The possibility of forming highly magnetized NSs of this kind was also shown in recent simulations [12, 13, 14]. Long-lived remnant NSs are important in the context of the “magnetar” [15, 16] and “time-reversal” [17, 18] scenarios for SGRBs (see [19] for an alternative proposal). These scenarios are also supported by the observation of long-lasting X-ray plateaus in the afterglow emission of many SGRBs [20].

Lifetime estimates of SMNSs based only on the total mass are necessarily very broad. More detailed models would have to take into account the exact rotation profile of the remnant and its evolution. A frequently used assumption in models of merger remnants is the so called  $j$ -constant law, featuring a rapidly rotating core and a slower rotation in the outer layers of the star. However, a recent study [21] of the rotation profile in merger remnants found completely different rotation profiles, with a slowly rotating core and faster rotating outer layers. Further investigation of this important aspect is needed.

In order to study the different scenarios, it is necessary to perform fully general relativistic magneto-hydrodynamic (GRMHD) simulations of both “high-mass” and “low-mass” magnetized BNS mergers. Since the NS equation of state (EOS) is still largely unknown (in particular for the high-density region in the NS core) it is important to explore different models. In GRMHD there have been very few publications considering different EOSs. Most of them have considered a simple ideal-fluid EOS [22, 23, 24, 25, 6, 12, 13, 8], very few piece-wise polytropic approximations [7, 14], and only one a finite temperature tabulated EOS including neutrinos [26]. Moreover, all the simulations have considered only equal-mass magnetized BNSs (except [23], using however a simple ideal-fluid EOS).

In this paper we present our new set of GRMHD simulations describing both equal and unequal-mass models of magnetized BNSs. We considered both an “high-mass” system, that collapses promptly to a BH after merger, and “low-mass” systems that produce SMNSs. We used a piecewise polytropic approximation of the APR4 EOS including also thermal effects. In all cases we studied the impact of magnetic field evolution on the dynamics, the GW emission, formation of disks, and the possible connection with EM emission.

Our paper is organized as follows. Section 2 describes the initial data and the numerical methods used to evolve them. In section 3 we describe the general dynamics of these systems, the structure of the disks that are formed, the rotation profile of the merger remnants, the evolution of the magnetic field, the GW signals, and the ejecta. In section 4 we summarize our main results. Throughout the paper we use geometric units with  $c = G = M_{\odot} = 1$ , unless specified otherwise. Baryonic mass is defined as baryon number times a formal baryon mass of  $1.66 \times 10^{-24}$  g.

## 2. Setup

### 2.1. Numerical Methods

All the numerical simulations presented in this paper were carried out using the publicly available Einstein toolkit [27] (“Wheeler” release) combined with our fully GRMHD code `Whisky` [28, 25, 12]. The GRMHD equations are written in a flux-conservative form using the “Valencia” formulation [29] and then solved using high-resolution shock capturing methods. In particular, the fluxes are computed via the standard HLLC formula [30] at the boundaries between cells where primitive variables are reconstructed via the PPM scheme [31]. As in all GRMHD simulations, we enforce a positive rest-mass density  $\rho$  by imposing an artificial atmosphere with fixed density and zero 3-velocity. Our choice for the atmosphere density is  $\rho_a = 6.2 \times 10^6$  g/cm<sup>3</sup>, which is one order of magnitude lower than what was used in our previous GRMHD simulations [28, 25, 6, 12]. When a BH is formed, hydro variables are excised (set to the artificial atmosphere) inside a region bounded by the apparent horizon scaled down by a factor of 0.6. This is done in order to avoid failures during the conversion from conserved to primitive variables (see [28] for details).

In order to preserve the divergence-free character of the magnetic field, we evolve directly the vector potential using the modified Lorenz gauge [32, 33]. This guarantees

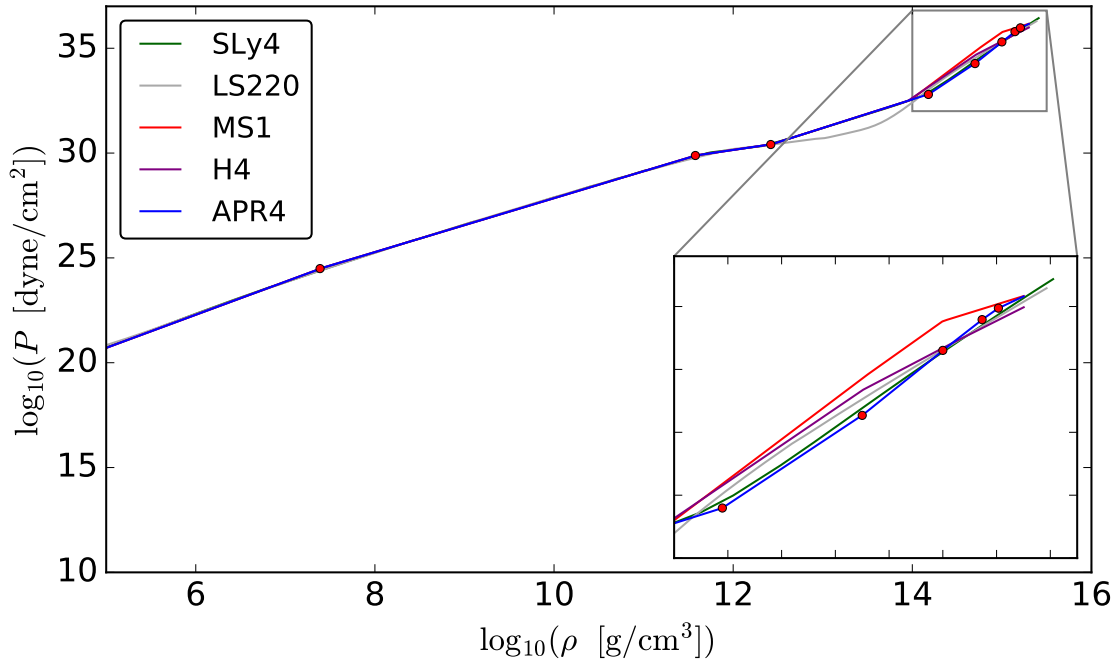


**Figure 1.** Pressure versus rest mass density relation for the piecewise polytropic approximation of the APR4 EOS used in this work. For comparison, we also show some other EOSs.

divergence-free magnetic fields and avoids spurious magnetic field amplifications at the boundary between refinement levels. Adaptive mesh refinement is implemented via the Carpet driver which is part of the Einstein toolkit. In all the simulations we employed 6 refinement levels, with a resolution of  $0.15M_{\odot} \approx 222$  m for the finest level. During inspiral, the two finest levels follow the NSs, which are completely contained in the finest grid. Shortly before merger, the moving grids are replaced by larger fixed grids. The smallest covers a radius of 30 km, sufficient to contain the post-merger remnant. The outer boundary is located at 794 km. In order to save computational resources, we apply reflection symmetry with respect to the equatorial plane. The Einstein equations are solved via the BSSNOK [34, 35, 36] formalism using the MacLachlan code, which is also part of the Einstein toolkit.

Our initial models are built using the publicly available LORENE library [37]. LORENE is a multi-domain spectral code that computes the initial data assuming a quasicircular orbit, an irrotational fluid-velocity field, and a conformally flat spatial metric.

## 2.2. Initial Data

All the initial data in this work employ a piecewise polytropic approximation of the APR4 EOS introduced by [38]. The parameters for the polytropic segments are taken from [39]. For the evolution, we add a thermal component to obtain a hybrid EOS given by

$$P(\rho, \epsilon) = P_{\text{cold}}(\rho) + (\Gamma_{\text{th}} - 1)(\epsilon - \epsilon_{\text{cold}}(\rho))\rho \quad (1)$$

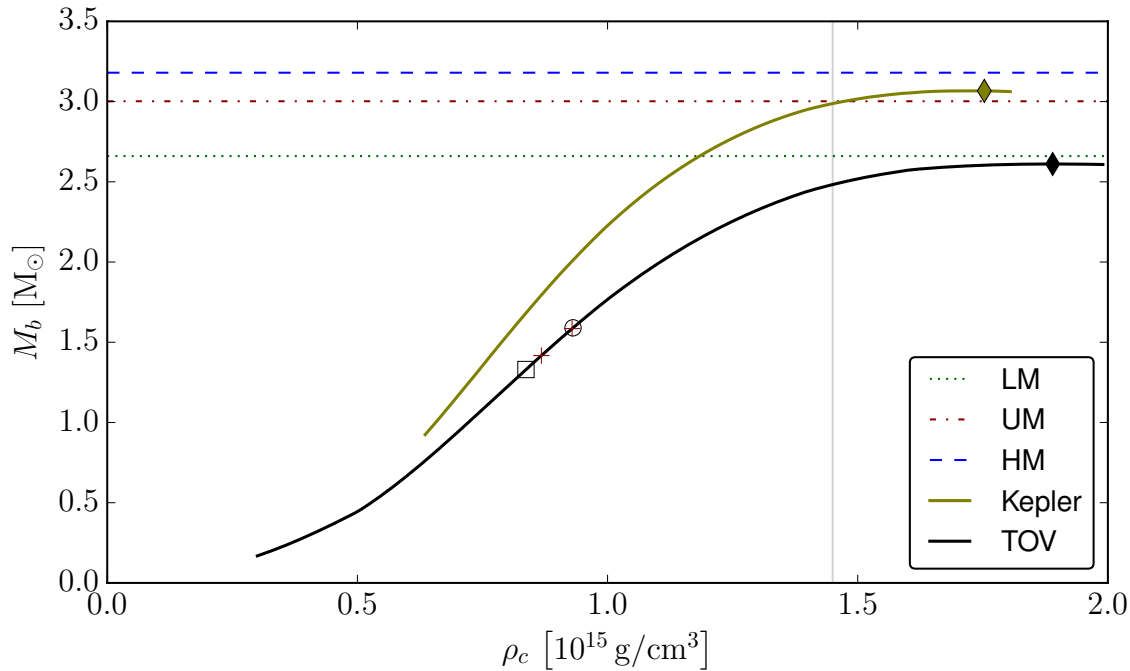


**Figure 2.** Total baryonic mass as function of the central rest mass density, for nonrotating NSs and for uniformly rotating NSs at the mass-shedding limit, employing the EOS used for all our initial data. The horizontal lines correspond to the total baryonic masses of the three models we evolved. The individual stars of the low-, unequal-, and high-mass binaries are marked by square, plus, and circle markers, respectively. The diamond symbols denote maximum mass models. The vertical line marks the density where the original APR4 approximation given in [39] becomes non-causal and had to be modified.

where we choose  $\Gamma_{\text{th}} = 1.8$  (see discussion in [40]). Further, we noticed that the piecewise polytropic approximation [39] of the APR4 EOS is only causal up to a density of  $1.45 \times 10^{15}$  g/cm<sup>3</sup>, above which the sound speed becomes superluminal. The critical density is larger than the central density of all the NSs used for our initial data. During the evolution however, the density can exceed this value, either during a short period when the stars are merging or while undergoing collapse to a BH. We therefore add two more high-density pieces, one with  $\Gamma = 3$  and starting at density  $1.4 \times 10^{15}$  g/cm<sup>3</sup>, and one with  $\Gamma = 2$  for densities above  $1.61 \times 10^{15}$  g/cm<sup>3</sup>. The resulting hybrid EOS is fully causal (regardless of temperature), although it is probably not particularly realistic in the high density part.

Figure 1 shows pressure versus rest mass density for the cold part in comparison to other well known EOSs. They differ only at high densities, since the EOS for the density range of the NS crust is better constrained by current understanding of nuclear physics. We should note that the same low density EOS is used together with the added thermal part for the evolution of ejected matter. Since such matter is shock-heated, we expect the thermal part to dominate in this regime. We computed sequences of TOV stars as well as uniformly rotating stars with maximal rotation using the piecewise polytropic APR4 EOS. Figure 2 shows the baryonic mass versus the central density for these sequences. We find that the supramassive

**Table 1.** Initial data parameters.  $M_b$  is the total baryonic mass of the systems,  $M_g$  is the gravitational mass of each star at infinite separation, and  $q = M_g^1/M_g^2$  the mass ratio.  $M_g/R_c$  is the compactness (dimensionless).  $f_0$  and  $d$  denote initial orbital frequency and proper separation, respectively.  $E_B$  is the initial magnetic energy of the magnetized models, which are otherwise identical to the non-magnetic ones.

Model	HM	LM	UM
$q$	1	1	0.905
$M_b [M_\odot]$	3.18	2.66	3.01
$M_g [M_\odot]$	1.43	1.22	1.29, 1.42
$M_g/R_c$	0.186	0.159	0.168, 0.186
$f_0$ [Hz]	288	270	282
$d$ [km]	60.0	57.5	59.0
$E_B [10^{42}\text{erg}]$	1.58	1.52	1.55

mass range lies between 2.61–3.07  $M_\odot$ .

We evolve three different initial models, which are summarized in table 1. The first (“high mass”, HM) is an equal mass model with total mass in the hypermassive range (cf. figure 2), which can either form a metastable HMNS or directly collapse to a BH. The second equal mass model is in the supramassive mass range and expected to form a long-lived remnant (“low mass”, LM). Our third model is an unequal mass binary with mass ratio 0.905 (“unequal mass”, UM). Although its total mass is in the upper supramassive regime, the resulting remnant can be somewhat lighter since unequal mass models typically form more massive disks during merger.

Each of the three models is evolved with and without an initial magnetic field. Since the LORENE code cannot yet compute magnetized BNS models, we manually add a poloidal magnetic field using a simple analytic prescription for the vector potential:

$$A_\phi \equiv \varpi^2 A_b \max(p - p_{\text{cut}}, 0)^{n_s}, \quad (2)$$

where  $\varpi$  is the coordinate distance to the NS axis (orthogonal to the orbital plane). The field is confined to the NSs, using a cutoff pressure  $p_{\text{cut}} = 0.04$  of the maximum (central) pressure. The exponent  $n_s = 2$  determines the degree of differentiability of the potential [25]. The strength of the field, determined by  $A_b$ , is chosen such that the maximum field strength is  $1.0 \times 10^{13}$  G. For the unequal mass model, this is done separately for each star. The corresponding magnetic energy (see table 1) is below  $10^{-11}$  of the NS binding energy. Hence we can neglect the impact on the hydrostatic equilibrium, and also the violation of the general relativistic constraints. We stress however that finding a stable magnetic field configuration for NSs is still an unsolved problem. The prescribed magnetic field topology will decay into an unordered field during the inspiral.

### 3. Results

In the following, we present the outcome of our simulations. Note that the results for the post merger phase lack reliable error estimates since convergence could only be demonstrated until

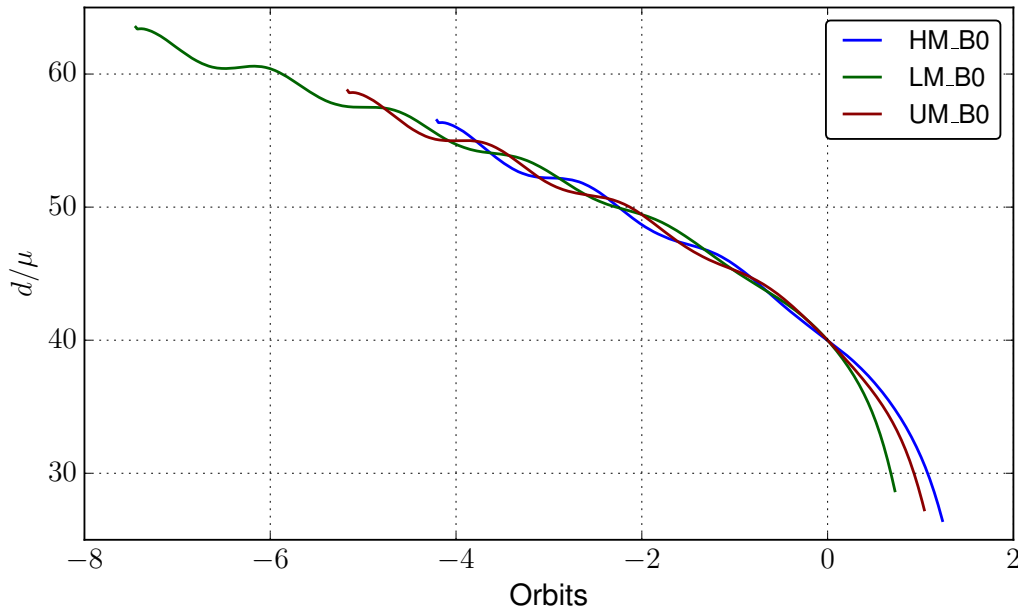


**Figure 3.** Proper separation between the centers of mass of the stars versus orbital phase. For each model, the separation is given in units of the reduced gravitational mass  $\mu$ . The orbital phases have been aligned to be zero at a separation of  $40 \mu$ .

merger. A detailed discussion of the numerical errors can be found in Appendix A.

### 3.1. General Dynamics

In the following, we provide an overview of the evolution of the three models. We will focus on the non-magnetic case. The influence of the magnetic field is very small and will be discussed in later sections.

The HM, UM, and LM models complete 5, 6, and 8 orbits before merger, respectively. The inspiral is depicted in figure 3 in terms of proper separation versus orbital phase. We recall that for point particles without spin and eccentricity, the separation scales with the reduced mass  $\mu = M_g^1 M_g^2 / (M_g^1 + M_g^2)$ , but also depends on the symmetric mass ratio  $\nu = \mu / (M_g^1 + M_g^2)$ . For the unequal mass model,  $\nu = 0.2494$ , which is very close to the value  $\nu = 0.25$  for equal masses. Ideally, the curves for all our models should only differ due to tidal effects. However, the differences during most of the inspiral are clearly dominated by the residual eccentricity of our initial data. Only during the last orbit, finite size effects become large enough to expose a trend: it seems that for the lighter models, the separation decreases more quickly with increasing orbital phase.

The evolution starting at the merger is visualized in figures 4, 5, and 6. All models tidally eject some matter shortly before the merger. Not surprisingly, the total ejected mass for the high mass model is negligible and the unequal mass model ejects more than the low mass model. This will be discussed in section 3.6. The high mass model undergoes prompt collapse to a BH upon merger. The BH mass and spin are given in table 2. The low- and

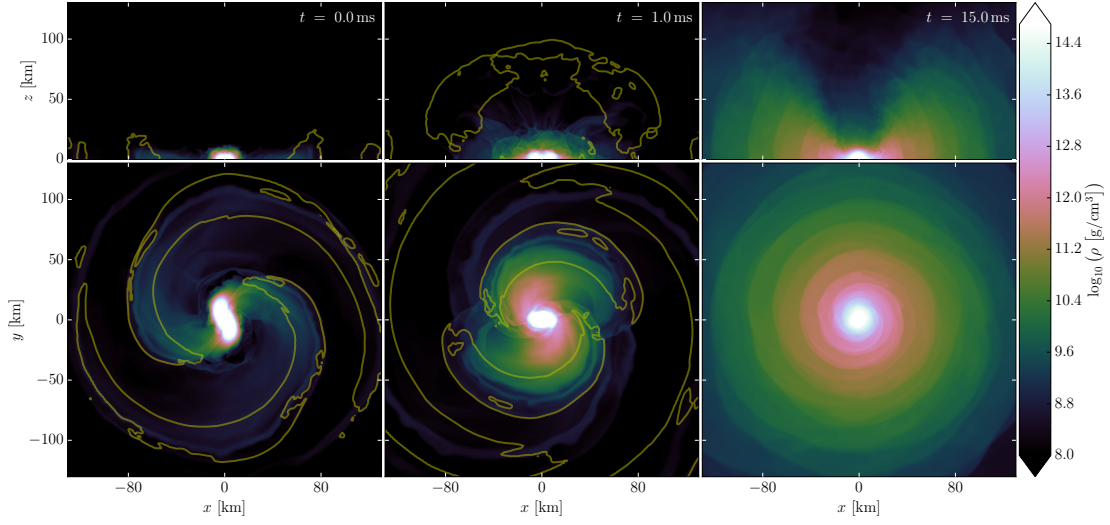


**Figure 4.** Snapshots of the evolution at 0, 1, and 15 ms after the merger, for model LM\_B0. The top row show cuts in the  $xz$ -plane, the bottom row cuts in the orbital  $xy$ -plane. The color corresponds to the logarithmic rest mass density. The contour lines mark the boundaries of regions where matter is unbound (according to the geodesic criterion).

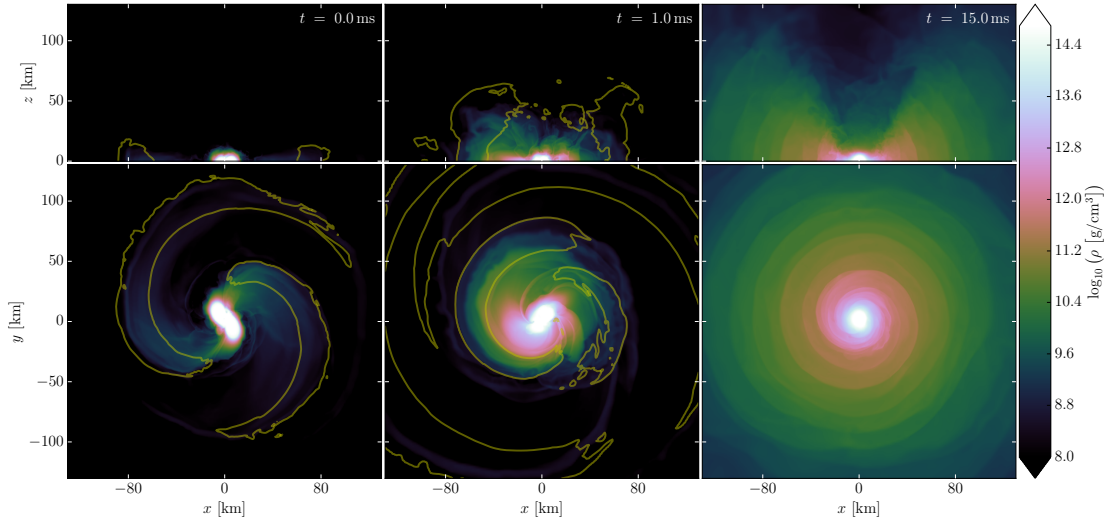


**Figure 5.** Like figure 4, but for model UM\_B0. In the lower left panel, showing the time of merger, the lighter star is on the lower right side of the origin.

unequal-mass models form supramassive remnants which are stable on the timescale of our evolution, i.e. for more than 15 ms.



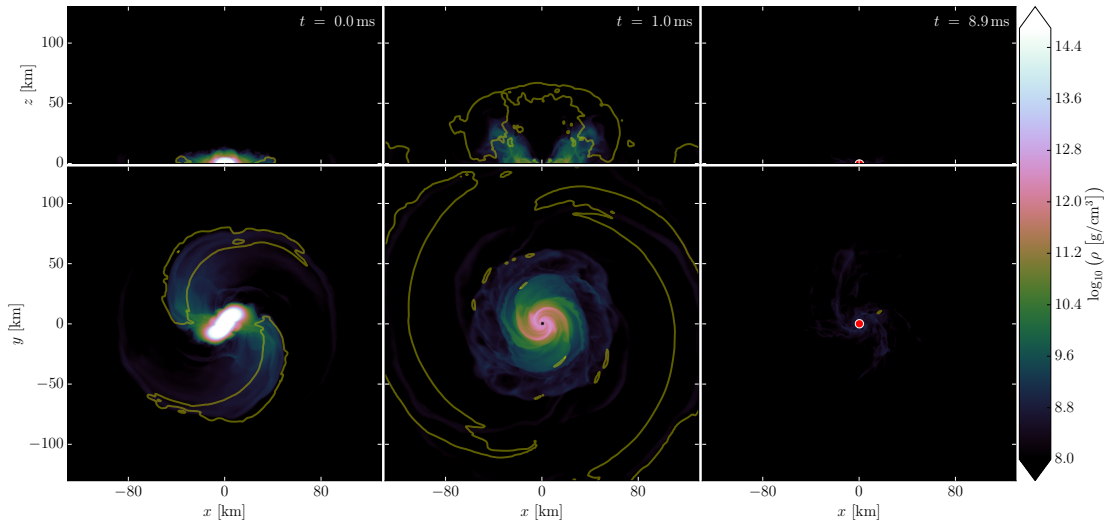


**Figure 6.** Like figure 4, but showing model HM\_B0. The apparent horizon and its interior are drawn in white and red, respectively.

### 3.2. Disk Structure

In the following, we will describe the distribution of bound matter outside the remnants. Unbound matter will be discussed separately in section 3.6. For the low- and unequal-mass models, the remnants are surrounded by heavy and thick Keplerian disks. As will be shown in section 3.3, the outer layers of the star already approach Keplerian velocity. The transition between star and surrounding disk is smooth (cf. figure 4).

At the end of our simulation, the bound mass still contains a significant fall-back component, i.e. matter that is moving along highly eccentric trajectories and will eventually fall back onto the remnant or the surrounding disk. In the equatorial plane, the fall-back component is mainly composed of tidally ejected matter. We found that its specific angular momentum is fairly constant. In detail, we compute the density-weighted  $\phi$ -average of specific angular momentum in the orbital plane,  $l(r)$ . For model LM\_B0, the average of  $l(r)$  taken over circumferential radii  $> 50$  km is  $l_f = 7.0 M_\odot$ . We found a very similar value of  $l_f = 7.2$  for model UM\_B0. For both, the  $L_1$ -norm of the residual is below 7% of  $l_f$ . The transition between disk and fall-back component is gradual. As a ballpark figure, we note that the angular velocity profiles for Keplerian motion and for constant specific angular momentum  $l_f$  cross each other at a circumferential radius of  $\approx 30$  km (the corresponding orbital period is around 2 ms). Further out, the fluid flow becomes gradually less stationary.

To quantify the mass distribution, we compute histograms of total and unbound baryonic mass (excluding artificial atmosphere) with bins corresponding to the coordinate radius. From this, we can compute the total bound mass outside a given radius. We also keep a histogram of proper volume, which allows us to define a volumetric radius  $r_v$  for the spheres of constant coordinate radius, thus reducing the gauge ambiguities.

**Table 2.** Outcome of the mergers.  $M_e$  is our best estimate for the total ejected mass, and  $v_{\text{esc}}$  the average escape velocity (see text).  $f_{\text{pk}}$  is the GW instantaneous frequency at merger time. If a BH is formed,  $M_{\text{BH}}$  and  $J_{\text{BH}}$  are its mass and angular momentum, extracted at the end of the simulations.  $M_f$  is the mass outside the apparent horizon. For the models without BH,  $F_c$  and  $F_m$  denote the remnant’s central and maximum rotation rates, computed 15 ms after the merger.  $M_d$  and  $M_f$  are tentative measures for disk and fall-back masses, respectively (see text). Finally,  $f_{\text{pm}}$  is the frequency of the largest peak in the post merger spectrum.

Model	HMB0	HMB13	LMB0	LMB13	UMB0	UMB13
$M_{\text{BH}} [M_{\odot}]$	2.79	2.79	—	—	—	—
$J_{\text{BH}}/M_{\text{BH}}^2$	0.78	0.78	—	—	—	—
$F_c$ [kHz]	—	—	0.52	0.49	0.67	0.66
$F_m$ [kHz]	—	—	1.50	1.54	1.63	1.60
$f_{\text{pk}}$ [kHz]	2.18	2.18	2.02	2.02	2.08	2.07
$f_{\text{pm}}$ [kHz]	—	—	3.17	3.14	3.30	3.26
$E_{\text{GW}} [M_{\odot}]$	0.039	0.039	0.053	0.056	0.087	0.080
$M_e [M_{\odot}]$	$< 10^{-3}$	$< 10^{-3}$	0.002	0.003	0.010	0.010
$v_{\text{esc}} [c]$	—	—	0.13	0.12	—	0.12
$M_d [M_{\odot}]$	—	—	0.130	0.091	—	0.119
$M_f [M_{\odot}]$	0.001	0.001	0.085	0.085	—	0.112

Although there is neither a clear distinction between disk and fall-back component, nor between remnant and disk, we provide in table 2 the mass  $M_d$  between  $20 < r_v < 60$  km as a tentative measure for the disk mass, and the mass  $M_f$  at  $r > 60$  km as a measure for the fall-back component (note that the value for model UM\_B0 is missing simply because the simulation was performed before the introduction of those measures). The disk masses given in table 2 are evaluated 15 ms after the merger. At this time, they are already stationary. On the timescale of our simulations, we observe no significant accretion onto the NS, and the expulsion of matter from the NS due to its oscillations ceases around 10 ms. Note that the remnants for the low mass models are in the mass range of stable NSs and will survive for at least an accretion timescale (but probably much longer).

The addition of the magnetic field apparently leads to a reduction of the disk mass by  $\approx 31\%$  for the low-mass models (see table 2). However, the disk masses directly after the merger are almost identical. The differences only appear around 5 ms after the merger. At this point, the mass ejection seems to be very sensitive to small changes, such as the presence of a magnetic field. The impact of the magnetic field on the specific angular momentum of the fall-back matter is very weak:  $l_f$  changes less than 1% (2%) for the low-mass (unequal mass) models.

In the high mass case, most material is swallowed immediately at merger time when the BH is formed. The total mass remaining outside the horizon at the end of the simulation is around  $10^{-3} M_{\odot}$ .

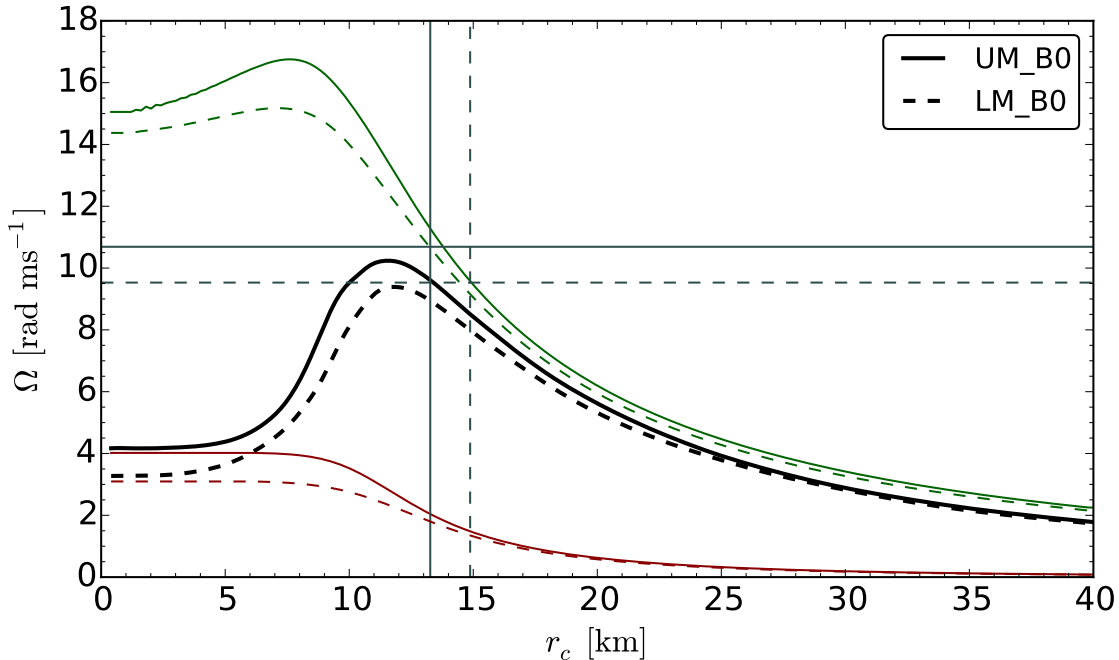


**Figure 7.** Rotation profiles after the remnant has settled down, averaged in time 14 . . . 18 ms after the merger. The thick black lines are the  $\phi$ -averaged rotation rates in the equatorial plane versus the circumferential radius. The red lines show the contribution of the frame dragging effect. The green lines show the orbital angular velocity of a test particle in circular, co-rotating orbit. The grey horizontal line marks the pattern angular velocity of the  $m = 2$  component of the multipole decomposition of the mass density in the equatorial plane. The grey vertical line marks the radius where the density drops to 5% of the central one.

### 3.3. SMNS Rotation Profile

In the following, we discuss the rotation profile of the remnant. In particular, we are interested in understanding how strongly the presence of the magnetic field affects the evolution of differential rotation.

To extract the rotation profile in a well defined way, we use the coordinate system introduced in [21], which is defined by a prescription independent of the spatial gauge used in the numerical evolution. However, the prescription still requires the choice of the origin. If the spacetime is approximately axisymmetric around the origin, the resulting coordinate system will reflect that fact, with  $\phi$  coordinate lines approximating Killing vectors. For our purpose, the origin should obviously be located at the center of rotation of the remnants. For equal mass models, the symmetry axis defines an origin in a gauge independent way. For the unequal mass models, we need to compensate for the residual movement of the remnant. Therefore, we use the center of mass (CMS) computed in simulation coordinates as the origin. Note that the CMS, and hence our choice of origin, is not a gauge invariant definition, and in contrast to the Newtonian case oscillations can weakly influence the CMS position. In order to prevent any feedback of oscillations, we use the running average in time of the CMS

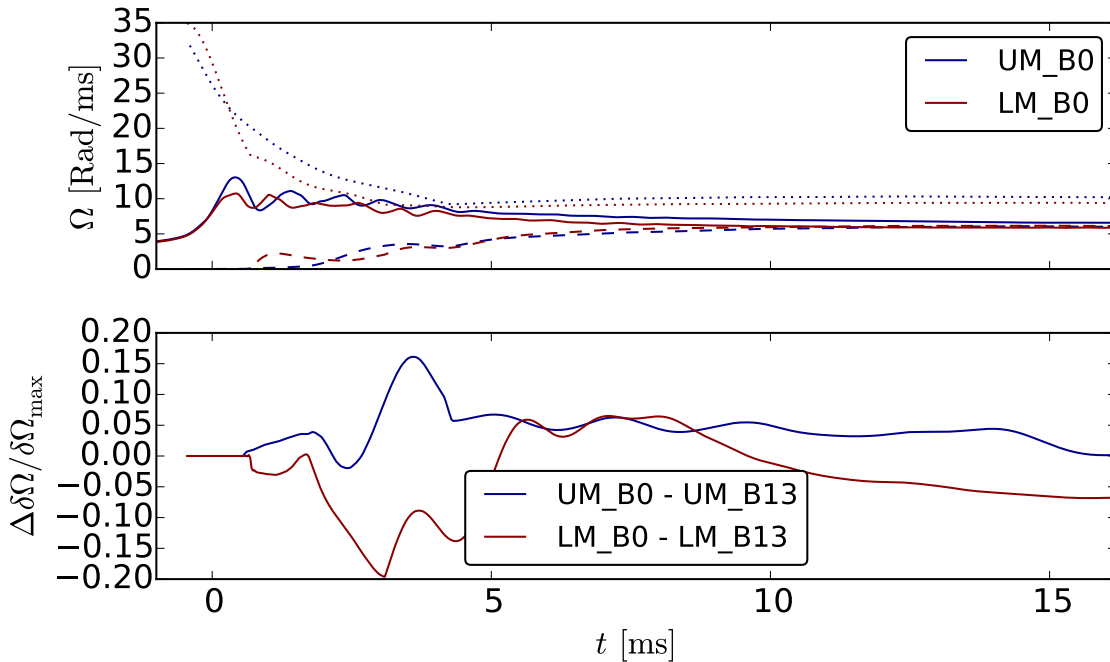


**Figure 8.** Evolution of rotation profile properties. The solid line shows the average rotation rate (see main text). The dotted line shows the central rotation rate, starting at the time the two stars touch (more precisely, when the central density reaches 5% of the maximum one). The dashed line shows the differential rotation in terms of the difference between maximum and central rotation rate. To highlight the overall evolution of central and differential rotation, we suppressed the influence of short term oscillations by smoothing in time via convolution with a Gaussian of width 0.5 ms.

position, with a smoothing length of 4 ms.

From our simulations, we obtain qualitatively similar rotation profiles as presented in [21] for different models. In particular, this applies also for the unequal-mass model, while [21] was restricted to equal-mass models. After the merger, the remnant settles down within a few ms to a state with a slowly rotating core, a maximum in the outer layers, and at larger radii a slow falloff towards the Keplerian velocity. This is depicted in figure 7. We note that directly after the merger, the maximum rotation rate is at the center. However, this configuration seems to be unstable and quickly changes towards the final profile. The nature of this transition is still under investigation, but it is likely connected also to the Kelvin-Helmholtz (KH) instability. It is worth noting that the pattern angular velocity of the  $m = 2$  moment of the density is very similar to the maximum of the rotation rate. This yet unexplained correlation was already observed in [21].

The rotation profiles for magnetized and non-magnetized models differ only slightly. The profile for the magnetized model UM\_B13 differs from the non-magnetized one depicted in figure 7 by less than 3.2%, with an average difference of 1.3%. In particular, differential rotation is not reduced significantly. Figure 8 depicts the evolution of the maximum rotation rate as well as the difference in rotation rate between the center and the maximum. The

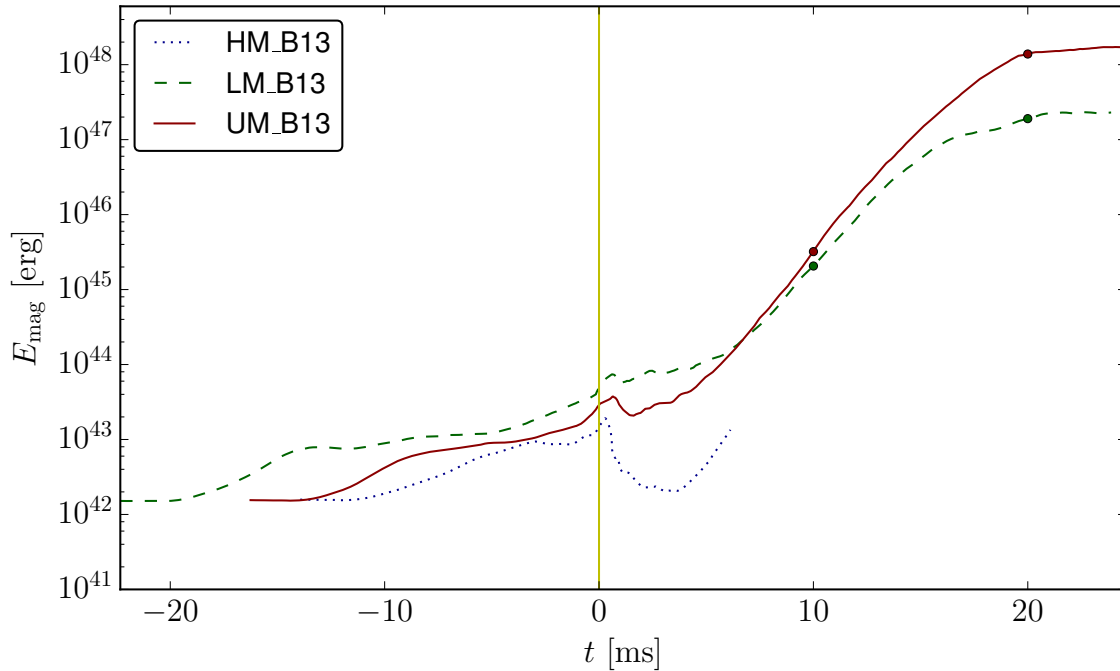


**Figure 9.** Evolution of the total magnetic energy for the three magnetized models: high-mass (blue dotted), low-mass (green dashed), and unequal-mass (solid red). The vertical line marks the time of merger  $t = 0$ . Circle markers indicate the times of the snapshots shown in figure 10.

differential rotation defined above is zero initially because the central rotation rate is also the maximum one at the merger. This changes rapidly, within  $\approx 5$  ms. Subsequently, the differential rotation keeps increasing slowly towards the final value. Note that the influence of the magnetic field seems to be stronger during the rapid rearrangement phase. This fits the conjecture that it is some sort of instability, and as such the exact time evolution would be sensible to the seed perturbations, but not the final state.

Figure 8 also contains the density weighted average of the rotation rate in the equatorial plane. During the first  $\approx 5$  ms after the merger, the rotation rate oscillates, with decaying amplitude. This is caused by the quasi-radial oscillations excited at merger, which change the moment of inertia periodically. Since rotation and differential rotation approach stationarity, we report the final values for all models in table 2.

### 3.4. Magnetic Field Evolution

We now turn our attention to the evolution of magnetic fields. Figure 9 depicts the evolution of total magnetic energy. As one can see, there is a moderate amplification already during the inspiral. There are several possible effects that might contribute to the evolution of the field. First, the chosen field configuration is known to be unstable and might re-arrange itself, which is however unlikely to amplify the field. A second possible cause could be fluid flows induced by tidal forces or GR effects, which is however purely speculative. A more likely cause is

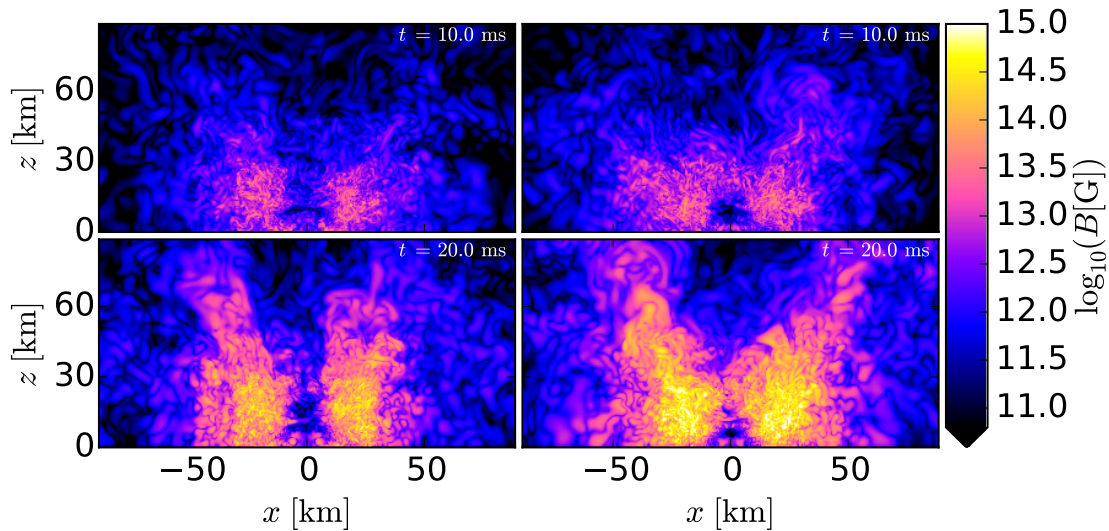


**Figure 10.** Meridional view of the magnetic field strength at selected times (10 and 20 ms after merger) for the low-mass model (left) and the unequal-mass model (right).

the imperfection of the initial data. The error due to the quasi-circular approximation might lead to some vortex-like, churning movements on top of more visible effects such as residual eccentricity and stellar oscillations. Numerical errors during the evolution can be ruled out as cause of the amplification, since we observe slightly more amplification during inspiral with better resolution, not less. In summary, we cannot tell if the amplification during inspiral is a generic feature or an artifact of our setup. In any case, we are not overly concerned about the changes during the inspiral since the actual field structure of BNS is completely unknown anyway and our setup is intended only as generic example of a magnetized merger. Moreover, we are confident that those changes do not influence the qualitative results in the post-merger phase which will be discussed in the following.

For the high-mass model, most of the matter and the associated magnetic energy is swallowed immediately at merger when the BH forms. The increase in magnetic energy a few ms after BH formation seems to be caused by the remaining low-density matter that is falling back onto the BH.

The magnetic energy of the low- and unequal-mass models undergoes an exponential growth phase after merger that lasts  $\sim 10$ – $15$  ms, with an e-folding time of  $\tau \approx 1.3$  ms. Around 20 ms after merger, the fields have reached a saturation. At this point, the magnetic energy in the unequal mass model has increased by almost five orders of magnitude compared to the energy at merger time. The main difference between the two cases is that the saturation amplitude we observe for the low-mass model is around one order of magnitude smaller. In addition, the growth rate is slightly lower. For the unequal-mass model, we performed a convergence test (see Appendix A), which showed that the magnetic field amplification is still under-resolved. For a higher resolution, we find a saturation amplitude that is larger by one order of magnitude.

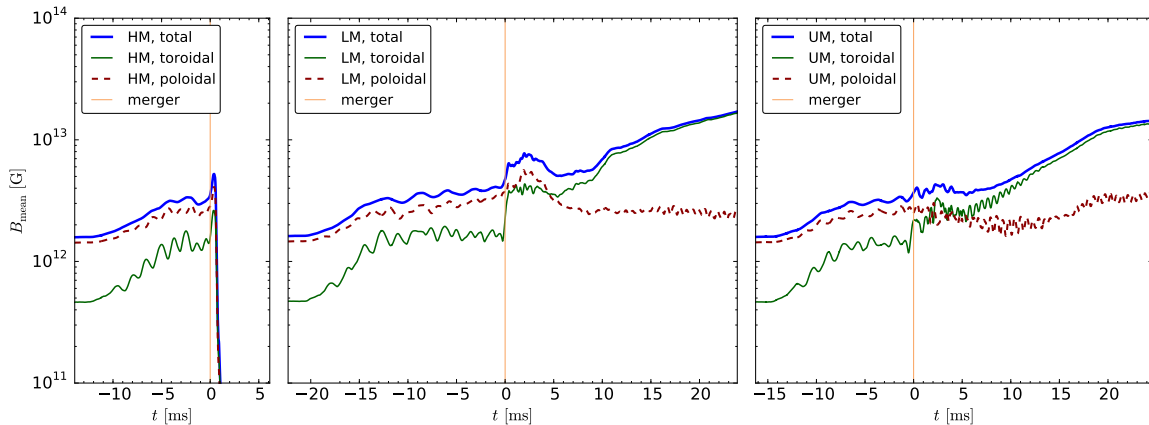


**Figure 11.** Evolution of the density-weighted average of the magnetic field strength (see text) for the three magnetized models: high-mass (left), low-mass (middle), and unequal-mass (right). In addition to the total strength (thick blue line), toroidal and poloidal field components are plotted (green and dashed red lines, respectively). The vertical line marks the time of merger  $t = 0$ .

The spatial distribution of the magnetic field strength in the meridional plane is depicted in Figure 10. It shows two snapshots, one at 10 ms, in the middle of the exponential growth phase, and one at 20 ms, when the fields have reached saturation amplitude. Interestingly, the field near the rotation axis is much stronger for the unequal-mass model than for the low-mass model. Also in relation to the field in the torus, the region near the axis is magnetized more strongly for the unequal mass case. The field is however unordered and not suitable to produce a jet. Furthermore, the level of baryon pollution along the axis differs. The rest-mass density along the axis can be up to one order of magnitude higher in the unequal-mass case (cf. figures 4 and 5).

As shown in figure 10, the maximum magnetic field strengths occur  $\sim 20$  km away from the orbital axis, a region with significant negative gradient of the angular velocity (cf. figure 7). Thus, magnetic winding should be at least partially responsible for the amplification. However, we found that toroidal and poloidal fields reach comparable strength in the torus. This might be explained by an unordered component of the fluid flow in the torus on top of the overall differential rotation, providing an effective redistribution of magnetic energy in the two components. Despite the amplification of magnetic fields, we find that the magnetic-to-fluid pressure ratio stays below  $10^{-2}$  everywhere up to the end of the simulation, indicating that magnetic fields remain always dynamically subdominant in our simulations (see Appendix B and figure A4).

As a measure for the evolution of the magnetic field inside the remnant, we use the density-weighted average of the magnetic field strength,  $B_{\text{mean}} \equiv \int \rho B dV / \int \rho dV$ . In the same way, we also compute the averages of the poloidal and toroidal components. The evolution of the averages is shown in figure 11 for the three magnetized cases (HM, LM, UM). As discussed earlier, there is already some amplification during the inspiral, which is most likely a consequence of our initial field choice. From figure 11, we find that the field

at merger is still mostly poloidal for all three models. Since the high-mass model promptly collapses into a BH, we only discuss the other two cases in the following.

After merger, the average magnetic field undergoes irregular variations for 3–5 ms and then it starts to increase continuously, although in the UM case it starts to saturate near the end of the simulation. The overall amplification in the remnant is much smaller than in the disk. At  $t = 20$  ms, the average field strength is larger by a factor  $\approx 3$  compared to the time of merger. In the LM case, we observe a steep temporary increase when the two stars touch. This might be due to the KH instability, which we expect to develop in the shear layer between the two stars, producing vortices in the orbital plane and amplifying the toroidal magnetic field component. However, it is difficult to draw conclusions from  $B_{\text{mean}}$  directly after merger because the density also undergoes rapid changes during this period, thus changing the relative weight of different parts of the field. In the UM case, the evolution of the average magnetic field is smoother. Nevertheless, when repeating the simulation with a higher resolution, we found a temporary post-merger amplification by a factor  $\sim 2$  (see figure A3), more similar to the low-mass case in figure 11. Recent work confirmed that a resolution of few tens of meters or better (much higher than the one employed here) is required in order to properly resolve the small scales at which the KH instability is most effective [14]. Our results thus under-estimate the amplification due to the KH instability.

Magnetic winding on the other hand should be well resolved. Since the merger remnants are differentially rotating, as shown in figure 7, we expect an amplification of the toroidal field inside the SMNSs. Indeed, by comparing the density-weighted averages of poloidal and toroidal field shown in figure 11, we find that mainly the toroidal field is amplified inside the SMNS. Note that although the magnetic winding occurs at the expense of differential rotation, the rotation profiles are almost unaffected at the given field strength, as discussed in section 3.3.

In theory, the magneto-rotational instability (MRI) [41] is an additional powerful amplification mechanism that could act inside the bulk of the SMNS as well as in the accretion torus (e.g. [42, 7]), although our present resolution is insufficient to properly resolve the wavelength of the fastest growing MRI mode.

Our LM and UM simulations show no indication in favor of the formation of a relativistic jet or any kind of outflow along the orbital axis, suggesting that these systems could not be responsible for SGRBs. This is in agreement with the general expectation that, while the formation of a BH-torus system within  $\sim 100$  ms after merger could provide the necessary conditions to launch a relativistic jet, the formation of a long-lived remnant NS can hardly act as a SGRB central engine, mostly due to the strong baryon pollution along the orbital axis [43, 44, 45, 46].

As a side note, an alternative possibility is the formation of a relativistic jet at a later stage, when the SMNS eventually collapses to a BH, as envisaged in the “time-reversal” scenario [17]. Before a SMNS can collapse, it has to lose a significant fraction of its angular momentum. Apart from the angular momentum carried away via GWs after merger, a good fraction of the rotational energy can be emitted via spin-down radiation, powering a potentially strong and long-lasting EM signal. This signal constitutes a promising counterpart



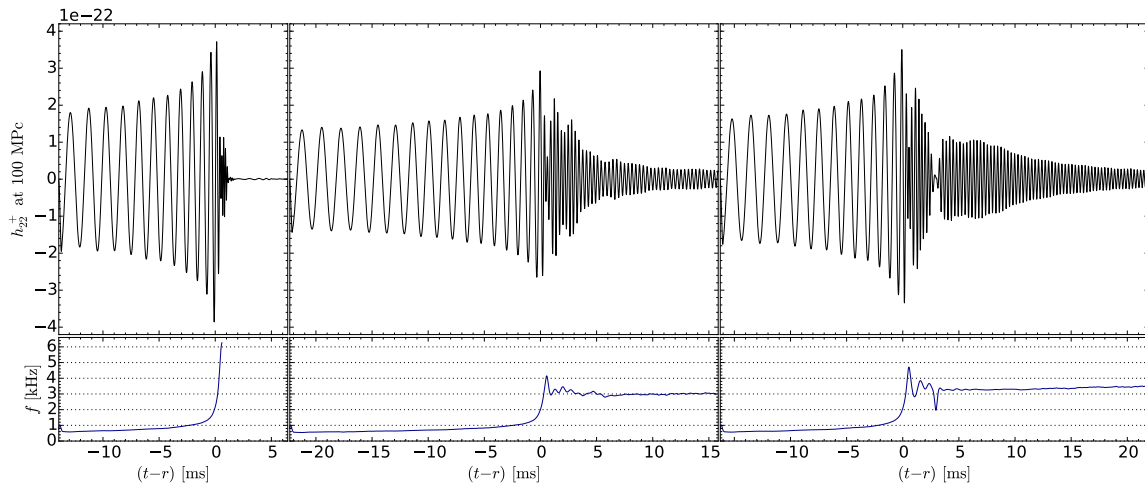


**Figure 12.** Gravitational wave signal for models HM\_B0, LM\_B0, and UM\_B0 (from left to right). The top panels show the strain at nominal distance of 100 Mpc. The lower panels show the instantaneous frequency.

to the gravitational wave emission from BNS mergers (see [47, 48] and references therein).

We stress again that due to the under-resolved KH and MRI mechanisms, the field amplification we observe can only act as a lower limit. In particular, KH instability is resolved, but only for vortices with length scale around at least 5 times our resolution (see also [49], [25]). Smaller vortices would need higher resolution to contribute to the magnetic field amplification. Instead, a resolution  $\approx 100$  times higher would be necessary in order to start resolving the MRI and see its effects on magnetic field amplification. In particular, we cannot rule out jet formation completely, although we consider it unlikely for our models. In addition, the prescription for the initial field might lead to differences. For example, our magnetic fields are initially confined inside the stars, while the presence of a global poloidal field extending outside the stars prior to merger might favor the formation of a magnetic funnel [9].

### 3.5. Gravitational Wave Signal

We extract the GW signal for all runs at a fixed radius of 738 km, using the Moncrief formalism (we also use the Weyl scalar  $\Psi_4$  as a crosscheck). We perform no extrapolation to infinity, since the precision is likely limited by the accuracy of the hydrodynamic evolution. Throughout this section, the strain will be given in terms of the coefficients  $h_{lm}$  of the expansion in spin weighted spherical harmonics (see [50]), where  $h_{lm} = h_{lm}^+ + ih_{lm}^\times$ . The actual strain at a given viewing angle to the rotation axis is obtained by multiplication with the spin weighted spherical harmonic  $|_{-2}Y_{22}(\theta, \phi)|$ .

The  $l = m = 2$  component of the strain for the non-magnetized models is shown in figure 12. The high mass model collapses to a BH within 1 ms after merger, hence the GW signal consists mainly of the inspiral part plus a short BH ringdown. The low- and unequal-mass models do not collapse and exhibit a strong post-merger signal.

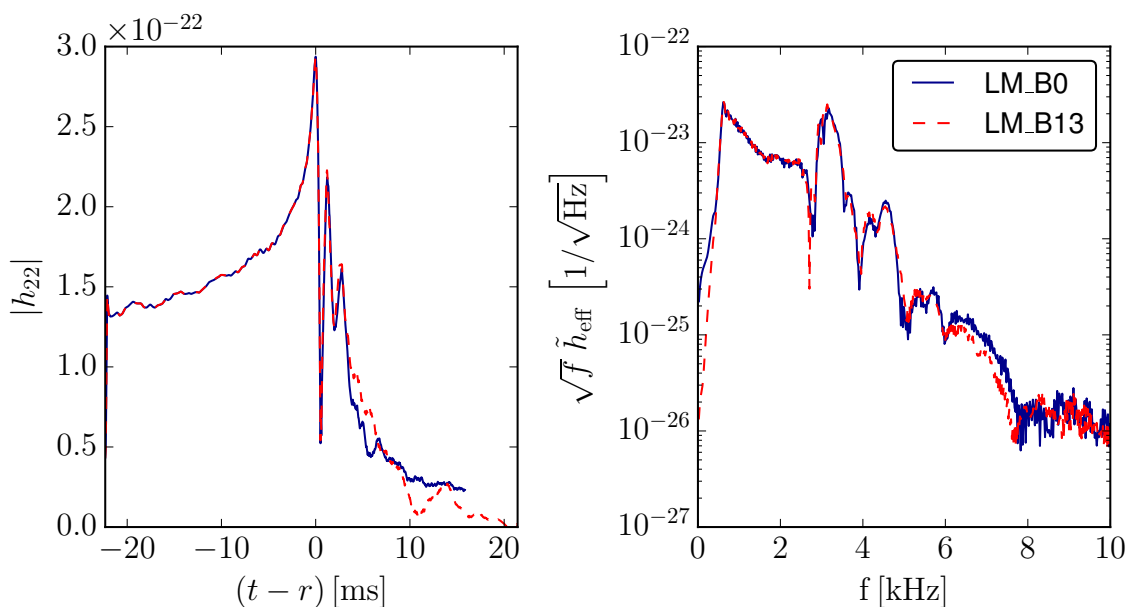


**Figure 13.** Influence of magnetic field on gravitational wave strain amplitude (left panel) and spectra (right panel) for the low-mass models. The strain is given at distance of 100 Mpc.

The other components of the strain are smaller than 7% of the dominant  $l = m = 2$  component in all cases. For the high mass model, the second largest contribution comes from the  $l = m = 4$  component, with a relative amplitude of 5.3%. The other components are smaller by a factor at least 5 apart from  $l = 3, m = 2$  which is only smaller by a factor 2. By comparing the spectra, we found that the  $l = 4$  component is just an overtone of the  $l = 2$  component, i.e. the peak frequency matches. For the low-mass model, the  $l = m = 4$  component has a relative amplitude of 4.1%. More interesting, we observe a growing  $l = m = 3$  component after the merger. Its maximum amplitude is 1.2 of the  $l = m = 4$  maximum, but it is reached 29.2ms after the merger.

The differences in the strain between magnetized and non-magnetized models during the inspiral are negligible. This is not surprising since the energy in the magnetic field in the orbiting NSs is below  $10^{-11}$  of a single star's gravitational binding energy. In the post-merger phase however, we observe some differences. For the unequal-mass model, the amplitude differs by up to 8% of the maximum one. The phase difference steadily grows up to 6 Rad at the end of the simulation. The knot visible in the amplitude is present in both cases. For the low-mass model, the strain amplitude for the magnetized model exhibits a knot  $\approx 10$  ms after the merger, which is not present in the non-magnetized case. This is shown in figure 13. At this time the difference in amplitudes is maximal, around 10% of the maximum amplitude (at merger time). Further, around the knot the phase shift quickly grows to around 3.5 Rad. The influence on the spectrum is however small, as shown in figure 13.

To track the time evolution of the dominant GW component, we compute its instantaneous frequency from the phase velocity of the complex strain  $h_{22}$ . To prevent amplifying high-frequency noise we use a Gaussian kernel derivative with smoothing length

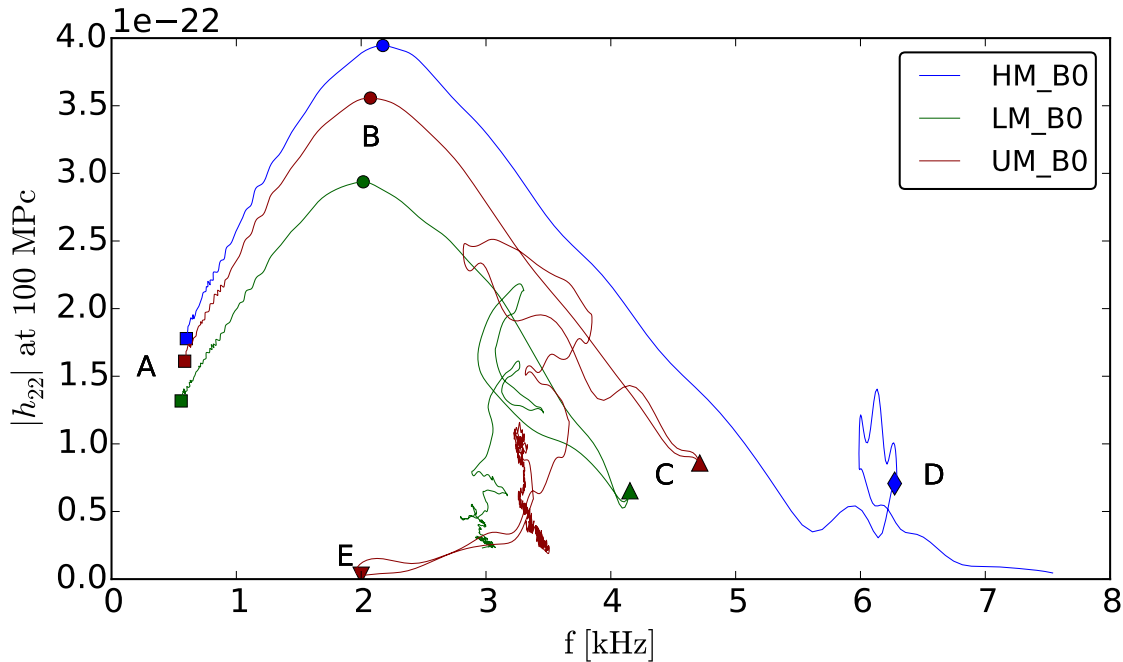


**Figure 14.** Gravitational wave amplitude  $|h_{22}|$ , versus the instantaneous frequency of the signal. The markers correspond to the following events: (A) Inspiral, (B) Merger, (C) Maximum frequency (not for prompt collapse), (D) Apparent horizon formation, (E) Knot in the GW signal for the unequal-mass model.

0.1 ms. The instantaneous frequency time evolution is shown in figure 12. In figure 14, we plot this frequency versus the strain amplitude. The evolution can be divided into several phases. During the inspiral (starting at points labeled A), both frequency and amplitude increase, the latter reaching a maximum when the stars merge. While the merged object becomes more compact, and hence rotates faster, the frequency keeps increasing. The amplitude on the other hand decreases again. This can be explained by the fact that the remnant becomes both smaller and more axisymmetric, hence reducing the quadrupole moment. For the high mass model, the system then undergoes collapse (point D marks the formation of the apparent horizon), during which the amplitude raises by a factor of 3 for a short time. The other models exhibit a bounce (points C). While the remnant expands again, both frequency decreases while the amplitude increases up to around 70% of the maximum amplitude. The low-mass model undergoes a second, smaller bounce. Afterwards, the oscillation frequency remains stable, while the amplitude decays slowly. The unequal-mass model shows a curious knot  $\approx 3$  ms after the merger (point E; note the instantaneous frequency at this point is meaningless because the amplitude of the dominant mode is close to zero, and the phase of the strain is hence determined by the other components and numerical errors). Around 5 ms after merger, however, the signal is that of one mode with decaying amplitude and slowly increasing frequency. We caution that the error for the GW amplitude after merger is unknown, since we could not demonstrate numerical convergence for the post-

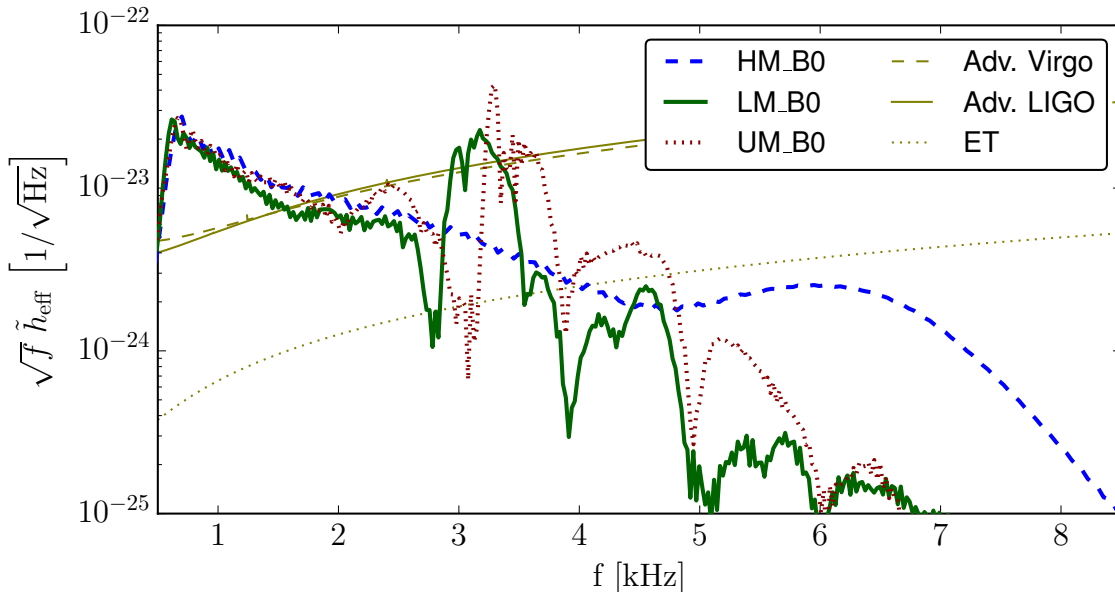


**Figure 15.** Gravitational wave spectra (thick lines) for the three models in comparison to the sensitivity curves of GW detectors (thin lines). The strain is given at distance of 100 Mpc.

merger GW amplitude (see Appendix A). We also note that the signal is missing the long-term evolution (not covered by the simulations), during which rotation rate, compactness, and frequency can still undergo slow, but significant drift.

We now discuss the power spectra of the GW signal, given by  $h_{\text{eff}}(f) = \sqrt{\tilde{h}_+^2(f) + \tilde{h}_\times^2(f)}$ , where  $\tilde{h}_+$ ,  $\tilde{h}_\times$  are the Fourier transforms of coefficients  $h_{22}^+(t)$ ,  $h_{22}^\times(t)$ . The spectra for all models are shown in figure 15, in comparison to the sensitivity curves of GW detectors. At a distance of 100 Mpc, the inspiral phase of all our models will be visible with both advanced LIGO and Virgo, while the post-merger part of the spectrum for the low- and unequal-mass models will be barely visible. Note that our signal does not include the long term evolution of the remnant. Although the amplitude at the end of our simulation is quite low, a longer integration time might enhance its detectability (e.g. [51, 52]). This depends on the damping at late times and the stability of the frequency. The high-frequency side-peak of the unequal mass models will be barely visible with the Einstein telescope, while the one produced by the low-mass models is too faint. The frequency of the largest post-merger peak of the spectra is given in table 2 for each model, together with the instantaneous frequency at merger time.

### 3.6. Matter Ejection

Computing the amount of ejected matter from numerical simulations is not straightforward for several reasons. First, it is very expensive to run the simulation long enough to let all ejected matter reach very large radii. We are therefore forced to apply approximate criteria to determine if a fluid element will eventually escape. There are two such criteria in use,

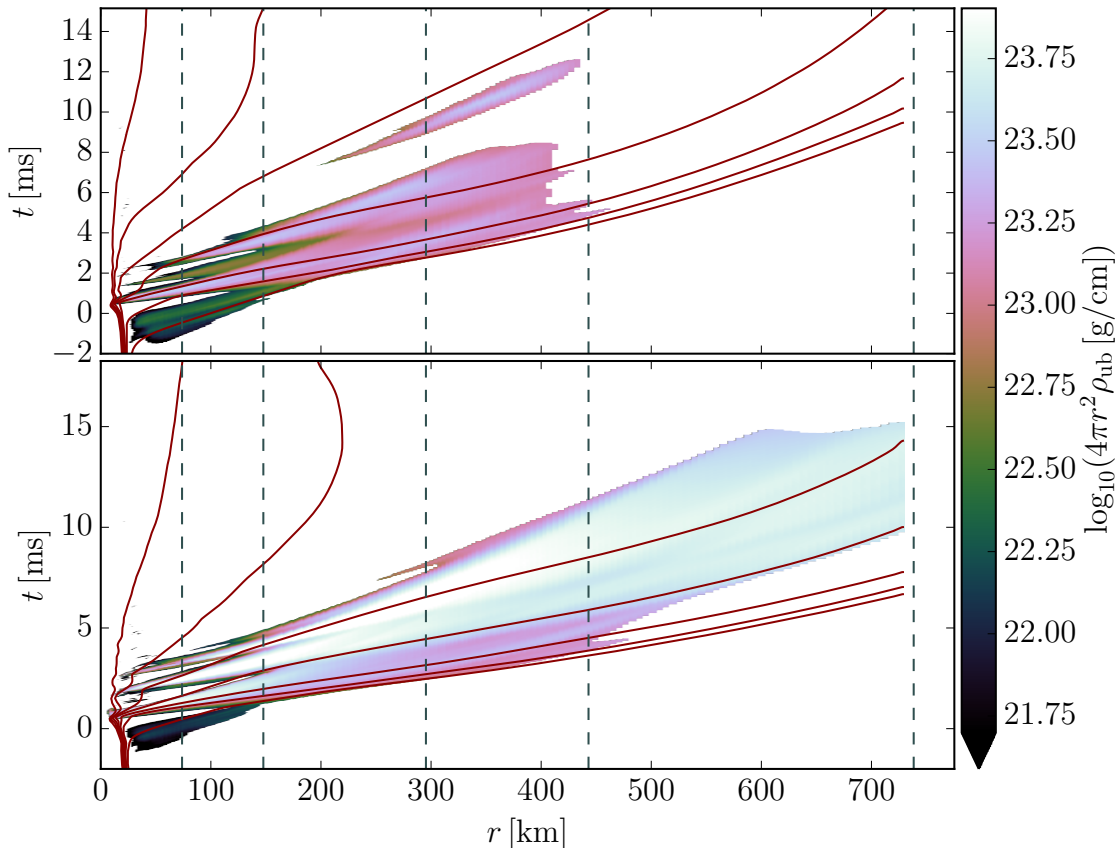


**Figure 16.** Distribution of matter versus radius and time, for models LM\_B13 (top panel) and UM\_B13 (bottom panel). The color corresponds to the amount of unbound matter in spherical shells per radius. Regions where the average density of unbound matter falls below the artificial atmosphere density are drawn in white. The total mass (excluding artificial atmosphere) outside a given radius is depicted with contour lines corresponding to  $10^{-n_i} M_{\odot}$ , where  $n_i = 1, 1.5, \dots, 4$ , from left to right. Note the contours in the lower panel become increasingly inaccurate after  $\approx 10$  ms due to matter reaching the boundary. The vertical lines mark the position of the spherical surfaces we use to compute mass fluxes.

both assuming a stationary spacetime. One is based on the assumption of geodesic motion, which leads to the condition  $u_0 < -1$ , where  $u_{\mu}$  is the fluid 4-velocity and we assume that the lapse is normalized to unity at infinity. The other is derived from the relativistic Bernoulli condition for stationary fluid flows, expressed by a similar condition  $hu_0 < -1$  (note  $h$  is only defined up to a constant factor, here we use the convention that  $h = 1$  for cold, infinitely diluted matter). The relativistic enthalpy  $h$  is larger than one, hence the Bernoulli condition always predicts a larger amount of unbound matter. In particular, the estimates increase with temperature.

Since the volume integral of the unbound mass according to both prescriptions is used in the literature, we made a comparison. The largest difference was found for model LM\_B0, where the Bernoulli criterion predicts around twice as much ejected mass. This can be attributed to the inclusion of shock-heated material. We consider the geodesic assumption

more realistic for our simulations since the ejected matter is launched in expanding shells which do not resemble a stationary fluid flow at all. It seems implausible that the thermal energy of a thin shell can be used to accelerate it outwards as it would be the case for fluid elements in a steady flow. In the rest of this section, we use the geodesic criterion. Of course, in the highly dynamic region near the remnant it is invalid as well.

A second problem is caused by the decreasing density of the outflowing matter, which eventually becomes less than the density of the artificial atmosphere used in our numerical scheme, causing loss of unbound matter at large radii. Fortunately, there is some freedom regarding the method for integrating the local measures to get the total amount of ejected matter, which we will exploit to minimize the influence of the above problems.

To map out the evolution of the radial matter distribution we compute at each time histograms of the amount of bound and unbound matter as well as proper volume, all versus coordinate radius. From this, we compute the average density of unbound matter at each radius, as well as the total amount of matter outside each radius. This is shown for two representative models in figure 16. As one can see, the average unbound matter density drops below the artificial atmosphere density before reaching 500 km for model LM\_B13. At this point, the measure becomes increasingly meaningless (although that also depends on the degree of spherical symmetry, with concentrated lumps of matter surviving longer). For model UM\_B13 on the other hand, part of the ejected matter escapes through the outer boundary.

Figure 16 also reveals that the matter is ejected in several waves, for both models. Using an animation, we identified the nature of each wave. For the unequal mass model, we find that the first wave is tidally ejected shortly before the stars touch. This wave has two arms, the one from the lighter star being slightly larger. It is relatively slow, contains very little matter, and is propagating in the orbital plane. The second wave is a combination of tidal ejection, expansion of the dense ejected matter, and shock waves. It is emitted in a more isotropic fashion and contains more matter. It is also faster, sweeping up the first wave. The third wave seems to be caused by shocks originating from the oscillating remnant. The situation for the low mass model LM\_B13 is qualitatively the same, apart from the asymmetry in the unequal mass case.

As indicated by figure 16, it can be difficult to find a time where all ejected matter is neither close to the source nor dissolving into the atmosphere. In this case, using volume integrals to estimate the ejected mass is problematic. A better option is the use of the unbound matter flux through spherical surfaces at a suitable radius, integrated in time. Since the best choice is unknown before the simulation, we monitor the fluxes through several surfaces, with radii  $r = 74, 148, 295, 443,$  and  $738$  km (cf. figure 16). We then use the surface yielding the maximum ejected mass for our best estimate. For the unequal mass models the corresponding radius is  $r = 443$  km, for the other models  $r = 295$  km. Additionally, we employ histograms like figure 16 to ascertain that the ejected matter at those radii are not too diluted.

Our best estimates are given in table 2, and a comparison of the different measures is shown in figure 17. Based on figures 16 and 17, we estimate the uncertainties for the ejected mass due to the extraction method to be around 30%. In addition, we expect an error due

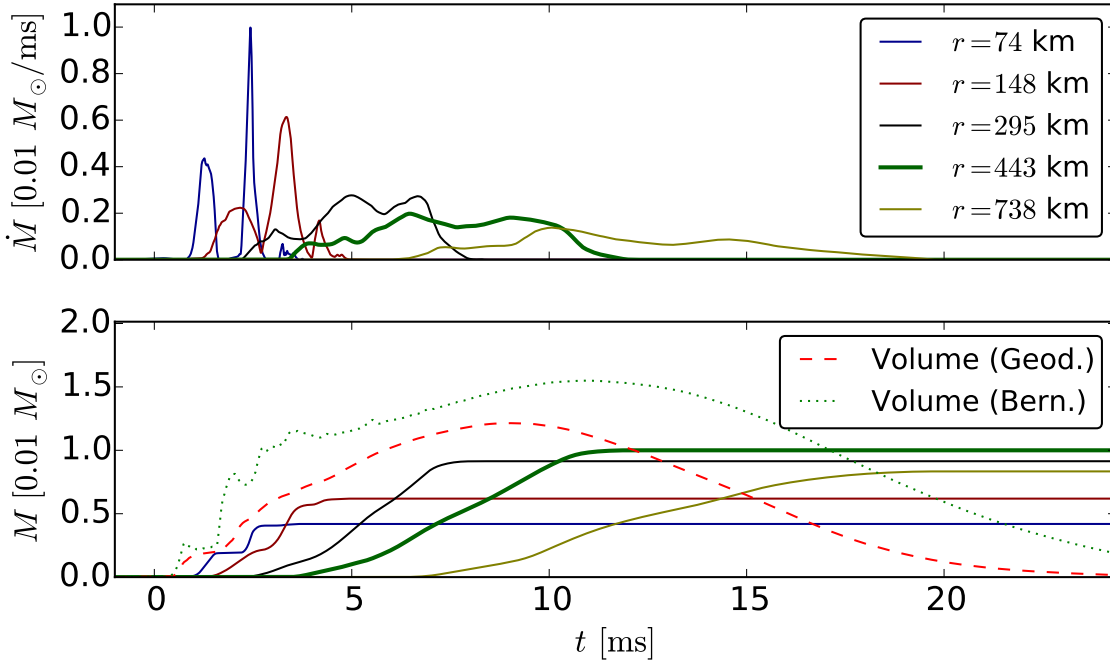


**Figure 17.** Comparison of different estimates for the unbound matter for run UM\_B0. The top panel shows fluxes of unbound matter, according to the geodesic criterion, through spherical surfaces at various radii. The bottom panel shows the time integrated fluxes from the top panel, and the volume integral over the computational domain for both geodesic and Bernoulli condition. The thick line is the one used for our best estimate.

to the finite resolution around 50%, as will be detailed in Appendix A. Not surprisingly, the high mass model shows no significant matter ejection, and we only provide an upper limit. As expected, the unequal mass model, although heavier, clearly ejects more matter than the low mass model.

To estimate the escape velocity, we compute an average escape Lorentz factor defined as  $W_{\infty} = -(\int u_0 \rho_u dV) / (\int \rho_u dV)$ , where  $\rho_u$  is the density of unbound matter and  $dV$  is the proper volume element. The integral is evaluated at the time when the volume integral of unbound matter reaches its maximum (compare figure 17). From this, we define the average escape velocity  $v_{\text{esc}} = \sqrt{1 - W_{\infty}^{-2}}$ . The results (except for run UM\_B0, which did not contain this measure) are given in table 2.

For the unequal mass model, we found no influence of the magnetic field. For the low mass models, which does eject only a small amount of matter in the first place, we observe a difference comparable to the numerical error. We also did not expect a significant impact, since the magnetic pressure is always less than  $10^{-2}$  of the fluid pressure, and even smaller at radii  $> 50$  km (see figure A4). We remark that on longer timescales  $\gg 100$  ms, baryon pollution in the environment surrounding a SMNS can be dominated by magnetically induced winds (e.g. [45]). Moreover, on such timescales neutrino induced winds can also contribute significantly (e.g. [43]). We also note that the amount of ejected matter might change when

considering initial NSs with spin, as shown in [21] for different equal mass models.

#### 4. Summary and Conclusion

We have presented a set of fully GRMHD simulations of BNS mergers employing the APR4 EOS, which include in particular the first GRMHD evolution of an unequal-mass BNS with a piecewise polytropic EOS. This set is meant to cover different scenarios for SGRB central engines: the “standard” one in which a BH is promptly formed (our HM case), and the “time-reversal” one [17] where a long-lived supramassive NS is the end result of the merger (LM and UM models). For all simulations, we have provided a detailed description of the dynamics, the magnetic field evolution, the ejected matter, the post-merger remnant properties, and the GW signals.

Both our UM and LM models produce massive disks orbiting the SMNS remnant, while in the HM model the mass left in the disk is negligible. Magnetic fields also have an impact on the disk mass, reducing it by  $\sim 31\%$ . All our SMNSs exhibit rotation profiles with a slowly rotating core, outer layers close to Kepler velocity, and a maximum in-between. This is similar to what was already observed in previous simulations [21] for equal mass systems with LS220 and NL3 EOSs. For the first time, we repeated the same detailed analysis of the rotation profile also for an unequal mass model, finding analogous qualitative results. Our findings suggest that our SMNSs are not supported against immediate collapse by the rotation of the core, but mainly by the centrifugal support of the outer layers. This can have crucial implications for the lifetime of the SMNS and for the possibility of forming a remnant disk after its eventual collapse.

In our simulations, magnetic fields do not grow stronger than  $\sim 10^{14}$  G and the ratio of magnetic to gas pressure remains always lower than  $\sim 10^{-2}$ . As a consequence, the impact on the dynamics is only marginal. Interestingly, the magnetic field in the SMNS (LM and UM cases) is strongly toroidal, while outside the post-merger remnant, both the toroidal and poloidal components have similar strengths. We also note that the UM case results in a larger amount of baryon pollution around the SMNS spin axis. The level of baryon pollution found in both the UM and LM case can easily choke the formation of a possible relativistic jet. This suggests that these systems are unlikely to act as SGRB central engines, unless the late-time collapse of the SMNS generates the conditions to launch a relativistic jet, as envisaged in the “time-reversal” scenario [17]. We remind the reader that our resolutions are not sufficiently high to accurately resolve the magnetic field amplification during the merger [14]. Future simulations employing higher resolution and/or our subgrid model [13] will be necessary to shed light on the impact of magnetic fields on the post-merger dynamics and possible jet formation.

For all models we also computed the GW signals. Not surprisingly, the magnetic field does not affect the GW signal during inspiral, but it has some small effects in the post-merger signal. Higher resolutions might result in stronger magnetic field effects. Placing our BNS mergers at a distance of 100 Mpc, we find that both advanced Virgo and advanced LIGO would have no difficulty in detecting the inspiral and merger GW signal, while the post-merger



signal of the LM and UM models would be barely visible. The detection of the post-merger GW signal would have crucial implications for the NS EOS, as it will clearly indicate the presence of an NS after merger and the frequency of the main post-merger peak can be used to constrain the EOS.

SGRBs are not the only EM counterparts that can be expected from these mergers. In the case of a SMNS remnant, the GW signal will be very likely accompanied/followed by a strong isotropic emission in the X-ray band, powered by the spindown of the NS [47, 48]. Moreover, our simulations of the unequal mass case show a large amount of unbound matter, around  $0.01 M_{\odot}$ , which could give rise to macronova emission. Some of this matter will also fall back at later times and hence provide a possible EM re-brightening of the central source.

Note that we use a simplified treatment of thermal effects instead of a finite temperature nuclear physics EOS (see [40] for a discussion of the accuracy of this approach) and that neutrino radiation is not included. Both will probably have an impact on the post-merger phase of the simulation. We consider this work as an intermediate step towards the implementation of a full description in our code and a useful basis for comparison.

When a post-merger GW signal will be detected with sufficient signal-to-noise ratio to extract the main frequency, or even the evolution of this frequency and the amplitude, numerical relativity simulations such as the ones presented in this paper will be crucial to interpret the findings and draw conclusions on the EOS. The same applies for a possible simultaneous detection of EM counterparts. Further, the availability of simulated GW signals will be beneficial for the development of better GW data analysis tools targeting BNS mergers. For these reasons, we will make all our gravitational waveforms publicly available, together with movies (available at [stacks.iop.org/CQG/33/164001/mmedia](http://stacks.iop.org/CQG/33/164001/mmedia)) visualizing the merger.

## Acknowledgments

We thank Luca Baiotti for useful discussions and comments. We also acknowledge support from MIUR FIR grant No. RBFR13QJYF. Numerical simulations were run on the cluster Stampede (TACC, USA) via XSEDE (allocation TG-PHY110027) which is supported by NSF grant No. OCI-1053575, on the clusters Fermi and Galileo at CINECA (Bologna, Italy) via INFN teongrav allocation and via ISCRA grants IsC34\_HMBNS and IsB11\_MagBNS, and on the cluster Datura at the Albert Einstein Institute (Potsdam, Germany). We also acknowledge PRACE for awarding us access to SuperMUC based in Germany at LRZ (grant GRSimStar). B.G. and T.K. also acknowledge partial support from “NewCompStar”, COST Action MP1304.

## Appendix A. Coverage Test

In order to estimate the accuracy of the numerical results, we evolved model UM\_B13 up to 15 ms after merger using three resolutions differing by a factor 1.25. The intermediate (“medium”) resolution  $dx = 221.5$  m is the one employed in all the other simulations in

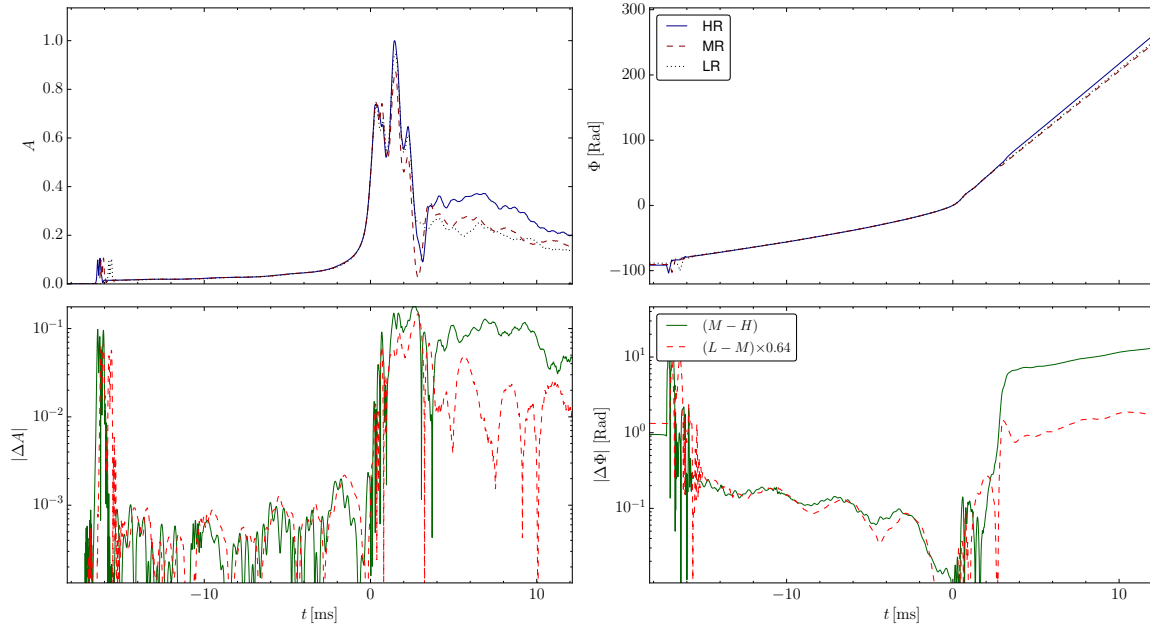


**Figure A1.** Comparison of GW signal obtained at resolutions  $dx = 177.2, 221.5, 276.9$  m. The top left panel shows the amplitude of the Weyl scalar  $\Psi_4$ , normalized to the maximum for the highest resolution. The time for each run is shifted such that the curves are aligned at time  $t_{\text{merger}}$ , the time when the strain reaches its maximum. The top right panel shows the (continuous) phase of  $\Psi_4$ , relative to the phase at  $t_{\text{merger}}$ . The bottom panels show the differences between consecutive resolutions. The low-medium residual has been scaled by a factor 0.64 that corresponds to the second order convergence we expect during inspiral.

this work. Figure A1 shows a comparison of the resulting GW signal. During inspiral, the errors converge, with an overall order around two, as expected from our scheme. During the merger, the convergence order drops to around one. We recall that the numerical scheme is only first order accurate when shocks are involved. The sharp raise around  $t = 3$  ms by  $2\pi$  in the difference of the continuous phases between medium and high resolution has a trivial explanation: the GW signal has a knot in the amplitude at this time, during which the phase is irrelevant, but very sensitive to errors. However, even when correcting for the phase jump, we cannot demonstrate convergence (of any order) after this point. Instead, we find a higher frequency and a much larger amplitude of the late GW signal when using high resolution compared to the low and medium resolution.

Before offering an explanation, we turn to the convergence of the maximum density shown in figure A2. During the inspiral, the density agrees very well. The differences that appear during merger are on average compatible with a convergence order of one. After 5 ms however, we start losing convergence, and the density for the high-resolution case continuously increases with respect to the lower resolutions. What causes this worrisome behavior? First, we note that the increase in central density seems to be a consequence of the decrease in angular momentum due to GW radiation. We already saw that the late GW amplitude for the high resolution run is larger. Compared to the medium resolution, the

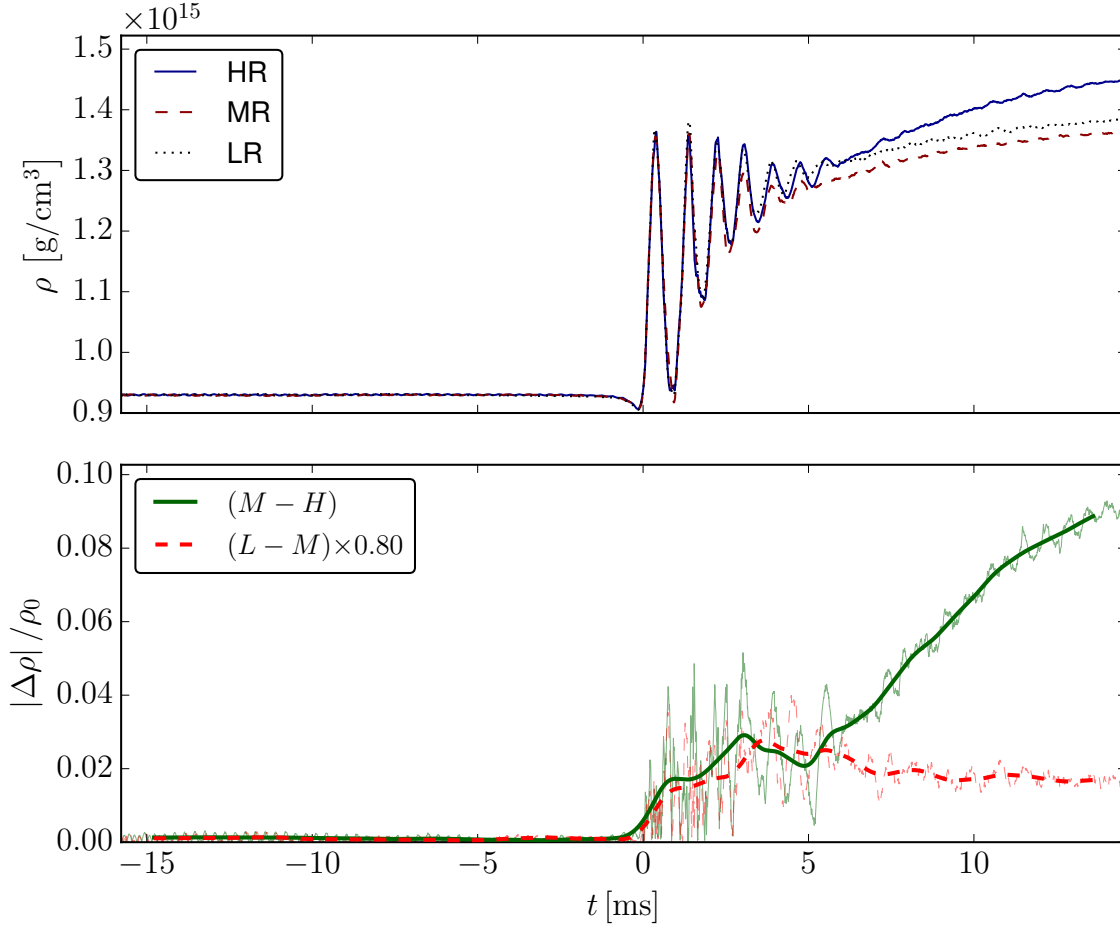


**Figure A2.** Upper panel: Evolution of the maximum rest mass density for the magnetized unequal-mass model. The different curves correspond to low, medium and high resolution. The time coordinate for each curve is relative to the time of the merger. Lower panel: Difference of maximum rest-mass density between consecutive resolutions, in units of initial maximum density (thin lines). As a measure of overall convergence, we also plot smoothed versions (thick lines). The low-medium residual was scaled by a factor 0.8 that corresponds to the first order convergence we expect during merger.

difference in radiated angular momentum is  $\Delta J \approx 0.08 M_{\text{ADM}}^2$ , which is enough to explain the difference in maximum density. The late time evolution more than 5 ms after merger can thus be explained by the differences of the remnant's  $l = m = 2$  oscillation mode amplitude which are already present a few ms after merger. We recall that the rotation profile undergoes some rapid rearrangement shortly after merger, which might be linked also to the KH instability. It seems very plausible that this also affects the oscillation amplitude. We therefore believe that the loss of convergence is mainly due to insufficient resolution during the short rearrangement phase, while the resolution at later times is sufficient. Given a fixed amount of computational resources, it might thus be beneficial to spend a larger fraction on this phase in order to reduce the overall error. In any case, it seems likely that the late evolution is as sensitive to small physical changes in the binary parameters as it is to the numerical error.

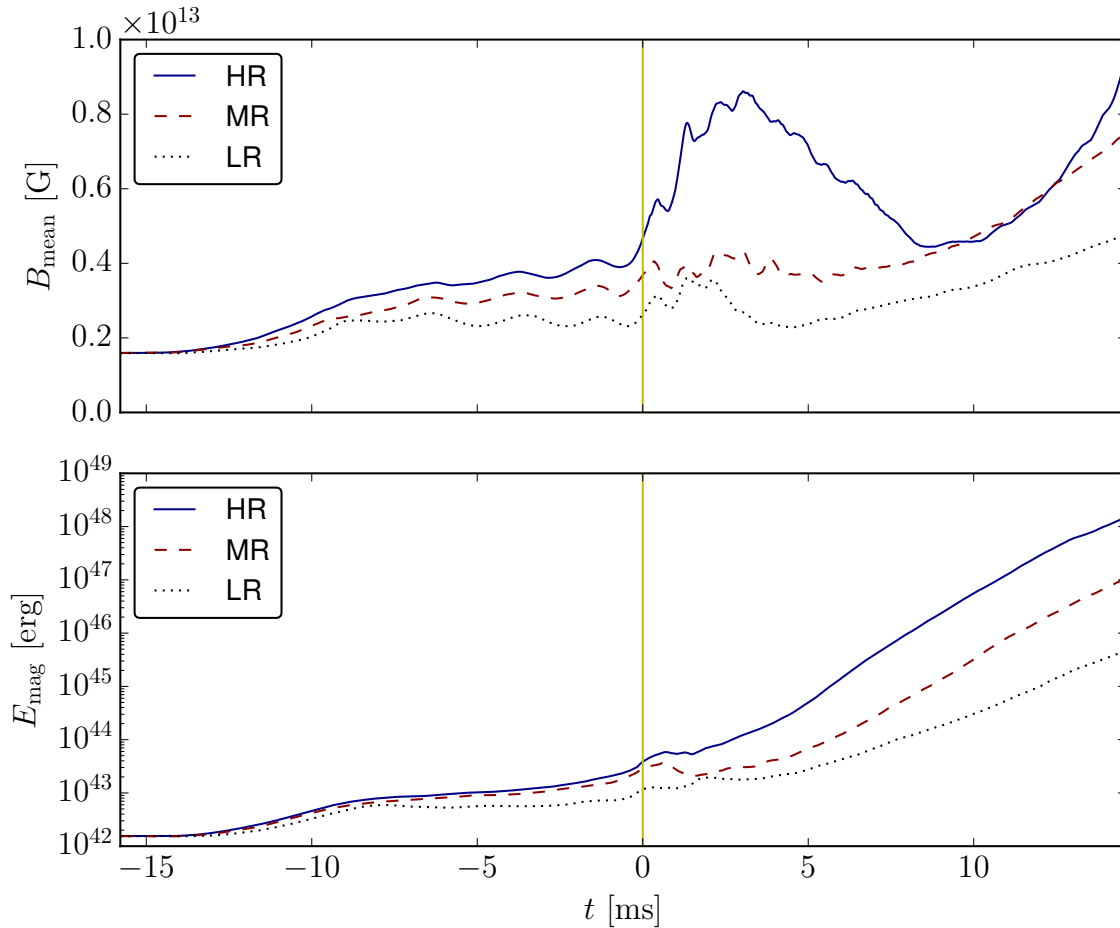


**Figure A3.** Evolution of the density-weighted average of the magnetic field strength  $B_{\text{mean}}$  (upper panel) and of the magnetic energy  $E_{\text{mag}}$  (lower panel) for the magnetized unequal-mass model. The different curves correspond to low, medium and high resolution. The vertical line marks the time of merger  $t = 0$ .

The mass of ejected matter obtained from the low-, standard-, and high-resolution runs is 0.0102, 0.0100, and 0.0090, respectively. Thus, we cannot demonstrate convergence for the ejecta mass. To estimate the error, we have to blame the lowest resolution. Making the optimistic assumption that we have first order convergence (as expected from our scheme in the presence of shock waves) starting from the standard resolution, we obtain an error of  $\approx 50\%$  for the ejecta masses obtained at the standard resolutions.

The evolution of the mean magnetic field strength  $B_{\text{mean}}$  (cf. section 3.4) and the magnetic energy  $E_{\text{mag}}$  is shown in figure A3. Convergent behavior is observed only up to the time of merger. In the post-merger phase, higher resolutions exhibit a much stronger magnetic field amplification. This agrees with the expectation (cf. section 3.4) that the important contribution to the amplification given by the KH instability, and possibly the MRI, act on length scales much too small to be fully resolved in our simulations. As a consequence, our results on the evolution of the magnetic field should be regarded as qualitative. In particular,

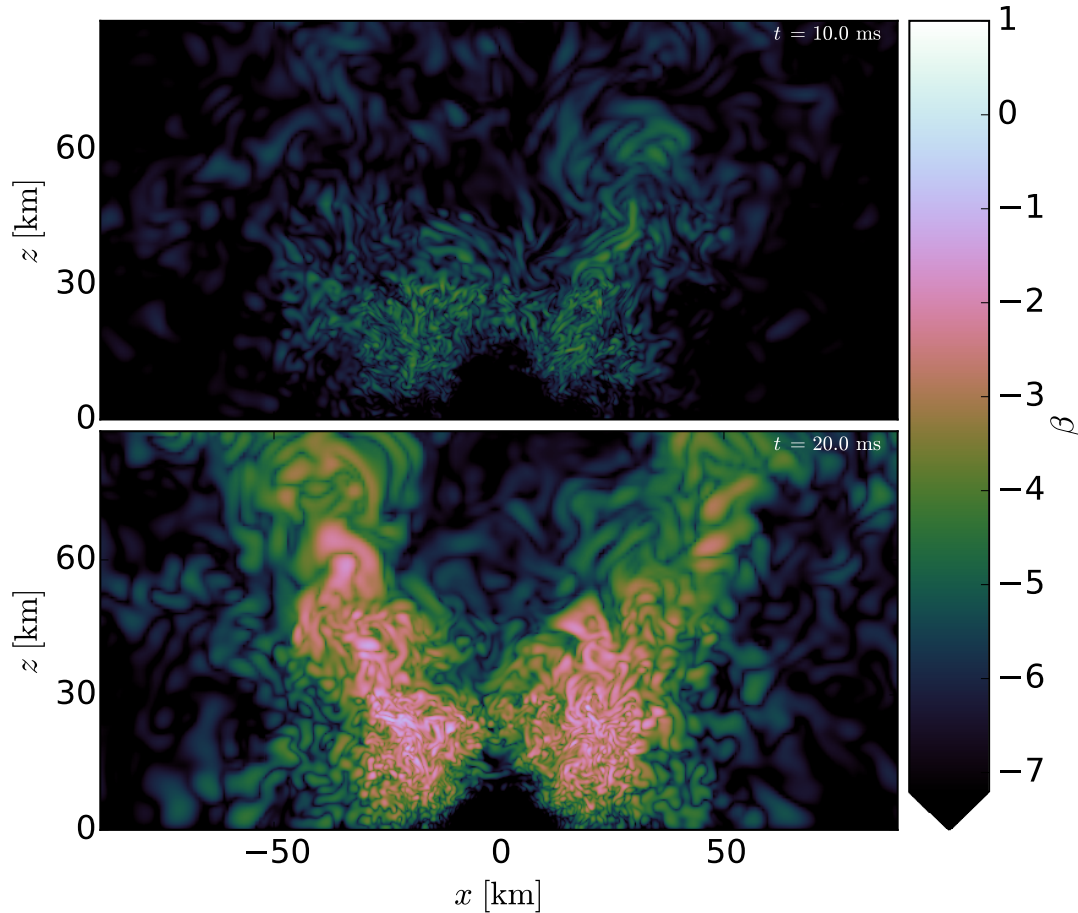


**Figure A4.** Meridional view of the magnetic-to-fluid pressure ratio (see text) for the magnetized unequal-mass model at  $t = 10$  and  $20$  ms.

the final level of magnetization reached as the system approaches a quasi-stationary state has to be considered as a lower limit. A more quantitative investigation, based on higher resolution simulations and/or on the use of a subgrid model [13] will be the subject of future work.

## Appendix B. Fluid pressure domination over magnetic field

In figure A4 we show the ratio of magnetic pressure over fluid pressure in the meridional plane for the unequal-mass case, 10 and 20 ms after merger. The ratio is defined as  $\beta \equiv b^2/2p$ , where  $b^2 \equiv b^\mu b_\mu$  and  $b^\mu$  is the 4-vector of the magnetic field as measured by the comoving observer [28]. We find that the maximum  $\beta$  is achieved in the torus and grows up to  $\sim \text{few} \times 10^{-2}$ . The growth of  $\beta$  is significantly slower towards the end of the simulation, following the behavior of the magnetic field amplification. We conclude that magnetic fields remain dynamically subdominant at all times and everywhere in the shown domain. The same conclusion applies to the other magnetized cases considered in this work.

## References

- [1] Abbott B P and et al (LIGO Scientific Collaboration and Virgo Collaboration) 2016 *Phys. Rev. Lett.* **116**(6) 061102 URL <http://link.aps.org/doi/10.1103/PhysRevLett.116.061102>
- [2] Abadie J, Abbott B P, Abbott R, Abernathy M, Accadia T, Acernese F, Adams C, Adhikari R, Ajith P, Allen B and et al 2010 *Classical and Quantum Gravity* **27** 173001 (*Preprint* 1003.2480)
- [3] Berger E 2014 *ARA&A* **52** 43–105 (*Preprint* 1311.2603)
- [4] Mendoza-Temis J d J, Wu M R, Langanke K, Martínez-Pinedo G, Bauswein A and Janka H T 2015 *Phys. Rev. C* **92**(5) 055805 URL <http://link.aps.org/doi/10.1103/PhysRevC.92.055805>
- [5] Korobkin O, Rosswog S, Arcones A and Winteler C 2012 *Monthly Notices of the Royal Astronomical Society* **426** 1940–1949 URL <http://mnras.oxfordjournals.org/content/426/3/1940.abstract>
- [6] Rezzolla L, Giacomazzo B, Baiotti L, Granot J, Kouveliotou C and Aloy M A 2011 *Astrophys. J.* **732** L6 (*Preprint* 1101.4298)
- [7] Kiuchi K, Kyutoku K, Sekiguchi Y, Shibata M and Wada T 2014 *Phys. Rev. D* **90** 041502 (*Preprint* 1407.2660)
- [8] Ruiz M, Lang R N, Paschalidis V and Shapiro S L 2016 *Astrophys. J. Lett.* **824** L6 (*Preprint* 1604.02455)
- [9] Paschalidis V, Ruiz M and Shapiro S L 2015 *Astrophys. J. Letter* **806** L14 (*Preprint* 1410.7392)
- [10] Demorest P B, Pennucci T, Ransom S M, Roberts M S E and Hessels J W T 2010 *Nature* **467** 1081–1083 (*Preprint* 1010.5788)
- [11] Antoniadis J, Freire P C C, Wex N, Tauris T M, Lynch R S, van Kerkwijk M H, Kramer M, Bassa C, Dhillon V S, Driebe T, Hessels J W T, Kaspi V M, Kondratiev V I, Langer N, Marsh T R, McLaughlin M A, Pennucci T T, Ransom S M, Stairs I H, van Leeuwen J, Verbiest J P W and Whelan D G 2013 *Science* **340** 448 (*Preprint* 1304.6875)
- [12] Giacomazzo B and Perna R 2013 *Astrophys. J. Letters* **771** L26 (*Preprint* 1306.1608)
- [13] Giacomazzo B, Zrake J, Duffell P, MacFadyen A I and Perna R 2015 *Astrophys. J.* **809** 39 (*Preprint* 1410.0013)
- [14] Kiuchi K, Cerdá-Durán P, Kyutoku K, Sekiguchi Y and Shibata M 2015 *Phys. Rev. D.* **92** 124034 (*Preprint* 1509.09205)
- [15] Zhang B and Mészáros P 2001 *ApJ* **552** L35–L38 (*Preprint* astro-ph/0011133)
- [16] Metzger B D, Quataert E and Thompson T A 2008 *MNRAS* **385** 1455–1460 (*Preprint* 0712.1233)
- [17] Ciolfi R and Siegel D M 2015 *Astrophys. J. Letters* **798** L36 (*Preprint* 1411.2015)
- [18] Ciolfi R and Siegel D M 2015 *PoS (SWIFT 10)* **108** Proceedings of "Swift: 10 Years of Discovery", Rome 2014 (*Preprint* 1505.01420)
- [19] Rezzolla L and Kumar P 2015 *ApJ* **802** 95 (*Preprint* 1410.8560)
- [20] Rowlinson A, O'Brien P T, Metzger B D, Tanvir N R and Levan A J 2013 *MNRAS* **430** 1061–1087 (*Preprint* 1301.0629)
- [21] Kastaun W and Galeazzi F 2015 *Phys. Rev. D* **91**(6) 064027 URL <http://link.aps.org/doi/10.1103/PhysRevD.91.064027>
- [22] Anderson M, Hirschmann E W, Lehner L, Liebling S L, Motl P M, Neilsen D, Palenzuela C and Tohline J E 2008 *Physical Review Letters* **100** 191101 (*Preprint* 0801.4387)
- [23] Liu Y T, Shapiro S L, Etienne Z B and Taniguchi K 2008 *Phys. Rev. D* **78** 024012 (*Preprint* 0803.4193)
- [24] Giacomazzo B, Rezzolla L and Baiotti L 2009 *MNRAS* **399** L164–L168 (*Preprint* 0901.2722)
- [25] Giacomazzo B, Rezzolla L and Baiotti L 2011 *Phys. Rev. D* **83** 044014 (*Preprint* 1009.2468)
- [26] Palenzuela C, Liebling S L, Neilsen D, Lehner L, Caballero O L, O'Connor E and Anderson M 2015 *Phys. Rev. D* **92** 044045 (*Preprint* 1505.01607)
- [27] Löffler F, Faber J, Bentivegna E, Bode T, Diener P, Haas R, Hinder I, Mundim B C, Ott C D, Schnetter E, Allen G, Campanelli M and Laguna P 2012 *Class. Quantum Grav.* **29** 115001 (*Preprint* 1111.3344)
- [28] Giacomazzo B and Rezzolla L 2007 *Class. Quantum Grav.* **24** S235 (*Preprint* gr-qc/0701109)
- [29] Anton L, Zanotti O, Miralles J A, Martí J M, Ibanez J M, Font J A and Pons J A 2006 *Astrophys. J.* **637** 296–312 (*Preprint* astro-ph/0506063)

- [30] Harten A, Lax P D and van Leer B 1983 *SIAM Rev.* **25** 35
- [31] Colella P and Woodward P R 1984 *J. Comput. Phys.* **54** 174
- [32] Etienne Z B, Paschalidis V, Liu Y T and Shapiro S L 2012 *Phys. Rev.* **D85** 024013 (*Preprint* 1110.4633)
- [33] Farris B D, Gold R, Paschalidis V, Etienne Z B and Shapiro S L 2012 *Phys. Rev. Lett.* **109**(22) 221102 URL <http://link.aps.org/doi/10.1103/PhysRevLett.109.221102>
- [34] Baumgarte T W and Shapiro S L 1998 *Phys. Rev. D* **59**(2) 024007
- [35] Shibata M and Nakamura T 1995 *Phys. Rev. D* **52** 5428
- [36] Nakamura T, Oohara K and Kojima Y 1987 *Prog. Theor. Phys. Suppl.* **90** 1–218
- [37] Gourgoulhon E, Grandclement P, Taniguchi K, Marck J A and Bonazzola S 2001 *Phys. Rev. D* **63** 064029 (*Preprint* gr-qc/0007028)
- [38] Akmal A, Pandharipande V R and Ravenhall D G 1998 *Phys. Rev. C* **58**(3) 1804–1828 URL <http://link.aps.org/doi/10.1103/PhysRevC.58.1804>
- [39] Read J S, Lackey B D, Owen B J and Friedman J L 2009 *Phys. Rev. D* **79**(12) 124032 URL <http://link.aps.org/doi/10.1103/PhysRevD.79.124032>
- [40] Bauswein A, Janka H and Oechslin R 2010 *Phys. Rev. D* **82** 084043 (*Preprint* 1006.3315)
- [41] Balbus S A and Hawley J F 1991 *ApJ* **376** 214–233
- [42] Siegel D M, Ciolfi R, Harte A I and Rezzolla L 2013 *Phys. Rev. D* **R 87** 121302 (*Preprint* 1302.4368)
- [43] Dessart L, Ott C D, Burrows A, Rosswog S and Livne E 2009 *ApJ* **690** 1681–1705 (*Preprint* 0806.4380)
- [44] Hotokezaka K, Kiuchi K, Kyutoku K, Okawa H, Sekiguchi Y i, Shibata M and Taniguchi K 2013 *Phys. Rev. D* **87** 024001 (*Preprint* 1212.0905)
- [45] Siegel D M, Ciolfi R and Rezzolla L 2014 *Astrophys. J. Letter* **785** L6 (*Preprint* 1401.4544)
- [46] Siegel D M and Ciolfi R 2015 *PoS (SWIFT 10)* **109** Proceedings of "Swift: 10 Years of Discovery", Rome 2014 (*Preprint* 1505.01423)
- [47] Siegel D M and Ciolfi R 2016 *Astrophys. J.* **819** 14 (*Preprint* 1508.07911)
- [48] Siegel D M and Ciolfi R 2016 *Astrophys. J.* **819** 15 (*Preprint* 1508.07939)
- [49] Baiotti L, Giacomazzo B and Rezzolla L 2008 *Phys. Rev. D* **78** 084033 (*Preprint* 0804.0594)
- [50] Thorne K S 1980 *Reviews of Modern Physics* **52** 299–340 URL <http://adsabs.harvard.edu/abs/1980RvMP...52..299T>
- [51] Dall’Osso S, Giacomazzo B, Perna R and Stella L 2015 *Astrophys. J.* **798** 25 (*Preprint* 1408.0013)
- [52] Gualtieri L, Ciolfi R and Ferrari V 2011 *Classical and Quantum Gravity* **28** 114014 (*Preprint* 1011.2778)